World Scientific Lecture Notes in Complex Systems – Vol. 4

editors

Michael Shats Herst Punzmann

Turbulence and Coherent Structures in Fluids, Plasmas and Nonlinear Media

**World Scientific** 

Lecture Notes on

# Turbulence and Coherent Structures in Fluids, Plasmas and Nonlinear Media

# WORLD SCIENTIFIC LECTURE NOTES IN COMPLEX SYSTEMS

Editor-in-Chief: A.S. Mikhailov, Fritz Haber Institute, Berlin, Germany

H. Cerdeira, ICTP, Triest, Italy

B. Huberman, Hewlett-Packard, Palo Alto, USA

K. Kaneko, University of Tokyo, Japan

Ph. Maini, Oxford University, UK

#### AIMS AND SCOPE

The aim of this new interdisciplinary series is to promote the exchange of information between scientists working in different fields, who are involved in the study of complex systems, and to foster education and training of young scientists entering this rapidly developing research area.

The scope of the series is broad and will include: Statistical physics of large nonequilibrium systems; problems of nonlinear pattern formation in chemistry; complex organization of intracellular processes and biochemical networks of a living cell; various aspects of cell-to-cell communication; behaviour of bacterial colonies; neural networks; functioning and organization of animal populations and large ecological systems; modeling complex social phenomena; applications of statistical mechanics to studies of economics and financial markets; multi-agent robotics and collective intelligence; the emergence and evolution of large-scale communication networks; general mathematical studies of complex cooperative behaviour in large systems.

#### Published

Vol. 1 Nonlinear Dynamics: From Lasers to Butterflies

Vol. 2 Emergence of Dynamical Order: Synchronization Phenomena in Complex Systems

Vol. 3 Networks of Interacting Machines

World Scientific Lecture Notes in Complex Systems – Vol. 4

editors
Michael Shats

Horst Punzmann

Australian National University, Australia

Lecture Notes on

# Turbulence and Coherent Structures in Fluids, Plasmas and Nonlinear Media



# **Preface**

The problem of turbulence and coherent structures is of key importance in many fields of science and engineering. It is an area which is vigorously researched across a diverse range of disciplines such as theoretical physics, oceanography, atmospheric science, magnetically confined plasma, nonlinear optics, etc. Modern studies in turbulence and coherent structures are based on a variety of theoretical concepts, numerical simulation techniques and experimental methods, which cannot be reviewed effectively by a single expert. The main goal of these lecture notes is to introduce state-of-theart turbulence research in a variety of approaches (theoretical, numerical simulations and experiments) and applications (fluids, plasmas, geophysics, nonlinear optical media) by several experts.

This book is based on the lectures delivered at the 19th Canberra International Physics Summer School held at the Australian National University in Canberra (Australia) from 16-20 January 2006. The Summer School was sponsored by the Australian Research Council's Complex Open Systems Research Network (COSNet).

The lecturers aimed at (1) giving a smooth introduction to a subject to readers who are not familiar with the field, while (2) reviewing the most recent advances in the area. This collection of lectures will provide a useful review for both postgraduate students and researchers new to the advancements in this field, as well as specialists seeking to expand their knowledge across different areas of turbulence research.

The material covered in this book includes introductions to the theory of developed turbulence (G. Falkovich) and statistical and renormalization methods (D. McComb). The role of turbulence in ocean energy balance is addressed in a review by H. Dijkstra. A comprehensive introduction to the complex area of the theory of turbulence in plasma (J. Krommes) is complemented by a review of experimental methods in plasma turbulence (M. Shats and H. Xia). An introduction to the main ideas and modern capabilities of numerical simulation of turbulence is given by J. Jimenez.

vi Preface

Experimental methods in fluid turbulence studies are illustrated in the lectures by J. Soria describing the particle image velocimetry. Finally, the relatively new field of the physics of vortex flows in optical fields is reviewed by A. Desyatnikov.

The Summer School in Canberra was accompanied by a workshop on the same topic. The Workshop Proceedings (editors J. Denier and J. Frederiksen) will also be published by World Scientific under the same title as these Lecture Notes ("Turbulence and Coherent Structures in Fluids, Plasmas and Nonlinear Media"). References in this book to the Workshop papers are given as "I. Jones, Workshop Proceedings".

Michael Shats Convenor of the 19th Canberra International Physics Summer School Canberra, August 2006

# Contents

Pr	Preface	
1.	Introduction to Developed Turbulence  Gregory Falkovich	1
2.	Renormalization and Statistical Methods $David\ McComb$	21
3.	Turbulence and Coherent Structures in the Ocean  Henk A. Dijkstra	81
4.	Analytical Descriptions of Plasma Turbulence $John\ A.\ Krommes$	115
5.	Experimental Studies of Plasma Turbulence  Michael Shats and Hua Xia	233
6.	The Numerical Computation of Turbulence  Javier Jiménez	281
7.	Particle Image Velocimetry - Application to Turbulence Studies	309

viii Contents

8. Vortex Flows in Optical Fields  $Anton \ S. \ Desyatnikov$ 

349

# Chapter 5

# Experimental Studies of Plasma Turbulence

# Michael Shats and Hua Xia

The Australian National University, Canberra ACT 0200, Australia E-mail: Michael.Shats@anu.edu.au, Hua.Xia@anu.edu.au

This chapter is based on two lectures given by M. Shats at the Summer School describing studies of turbulence in toroidal plasma confinement experiments. Some plasma diagnostics relevant for turbulence studies are reviewed. The data analysis techniques and methods are described in the context of the turbulence studies performed in the low-temperature plasma of the H-1 toroidal heliac, with particular emphasis on the analysis of spectral transfer in turbulent spectra. Experimental results on self-organization of the two-dimensional fluid turbulence are presented to illustrate some similarity with processes in quasi-two-dimensional plasma turbulence. Experimental signatures of zonal flows in plasma are illustrated.

# Contents

5.1.	introduction	4
5.2.	Experimental techniques and diagnostic tools in plasma turbulence 23	6
	5.2.1. Langmuir probes	6
	5.2.2. Characterization of turbulent transport using probes	9
	5.2.3. Collective (Bragg) scattering of electromagnetic waves by density fluc-	
	tuations	2
	5.2.4. Reflectometry in fluctuation studies	5
	5.2.5. Doppler reflectometry	6
	5.2.6. Optical imaging of turbulent fluctuations	7
	5.2.7. Heavy ion beam probe	9
5.3.	Spectral analysis techniques	0
	5.3.1. Higher-order spectral analysis	2
	5.3.2. Wave coupling equation	3
	5.3.3. Computation of the power transfer function	4
	5.3.4. Amplitude correlation technique	9
5.4.	Experimental evidence of the inverse energy cascade in plasma 26	1
	5.4.1. Applicability of the nonlinear spectral transfer model	1
	5.4.2. Results on the spectral transfer analysis	3

234

#### Michael Shats and Hua Xia

5.5.	Quasi-two-dimensional turbulence in fluids and plasma and generation of	
	zonal flows	26
	5.5.1. Spectral condensation of 2D turbulence	26
	5.5.2. Zonal flows in plasma turbulence	26
5.6.	Conclusion	27
Rihl	iography	27

#### 5.1. Introduction

Our interest in experimental studies of turbulence in magnetized plasma has been driven by the need to understand anomalously high loss of particles and energy across confining magnetic field in toroidal magnetic confinement experiments. Anomalous transport in plasma placed in magnetic field has been attributed to microscopic plasma turbulence as early as 1949 by Bohm<sup>1</sup> who suggested that oscillating electric fields due to plasma instabilities can substantially increase diffusion. Due to massive theoretical effort, large number of linear instabilities have been proposed as candidates for driving fluctuations in the plasma density and electrostatic potential (for review see e.g. <sup>2,3</sup>).

Experimental studies of the low-frequency (typically below 1 MHz) turbulent fluctuations in the high-temperature plasma in tokamaks initially focused on characterization of the small-scale density turbulence. Measurements of the frequency and wave number spectra of the density fluctuations in the high-temperature plasma regions were performed using scattering of the microwave<sup>4,5</sup> and laser<sup>6,7</sup> radiation. Experiments performed between 1976 and 1979 have revealed several important characteristics of the plasma turbulence, and have triggered theoretical work beyond linear theory of various instabilities.

One of them was the observation of the broad frequency and the wave number spectra at both the inner (high temperature) plasma regions and at the periphery. Spectra of developed plasma turbulence do not show any obvious features which correspond to an underlying linear instability and typically have maxima in the frequency (and wave number, k) range which is much lower than that of the expected linear (drift) instability. Some of these observations have been partially understood within the frame of simple nonlinear models, such as the Hasegawa-Mima (H-M) model. The analysis of the spectral evolution in the H-M model has shown the possibility of the dual cascade via the three-wave interactions and the transfer of energy and potential enstrophy in k-space (see also Chapter 4.4. by J. Krommes). This process was found to be similar to the energy and enstrophy cascades in two-dimensional (2D) Navier-Stokes turbulence (see

September 20, 2006 13:20

Chapter 1 by G. Falkovich). The inverse energy cascade in the plasma turbulence, similarly to the 2D fluid turbulence, tends to condense at low k. As a result, a potential structure is formed whose poloidal component of the wave vector is small,  $k_{\theta} \approx 0$ , while its radial component  $k_r$  is finite. Such structures are referred to as zonal flows.<sup>9</sup>

Zonal flows have been studied theoretically and in numerical simulations (for review see<sup>10</sup>). Recently several experimental reports on observations of zonal flows<sup>11–17</sup> have confirmed basic theoretical predictions and demonstrated the universality of zonal flows. Zonal flows may play many important roles in magnetically confined plasma, such as the regulation of the drift-wave turbulence,<sup>18</sup> formation of the transport barriers<sup>19</sup> and others.

Detailed experimental studies of the zonal flow - turbulence interaction have become possible due to the remarkable progress in diagnostics for turbulence studies, such as the heavy-ion beam probe, the Doppler reflectometry, beam emission spectroscopy, and others. More traditional fluctuation diagnostics, such as the Langmuir probe arrays in combination with modern signal analysis techniques also contributed to improved understanding of the plasma turbulence.

The main goal of these lectures given at the Summer School by M. Shats is to introduce some aspects of turbulence in toroidal magnetized plasma from experimental point of view. Though it is impossible in two lectures to even mention all plasma diagnostics relevant to the turbulence studies, we will select several diagnostics, which in our view, have significantly contributed to the progress in understanding plasma turbulence in recent years. This selection is highly subjective, nevertheless it gives a feeling about the direction in which experimental plasma turbulence studies are moving.

In Section 2, we describe some experimental techniques for studying turbulence in magnetized plasma, such as the Langmuir probes, collective scattering of electromagnetic waves by the density fluctuations, reflectometry, the Doppler reflectometry, beam emission spectroscopy, and the heavy-ion beam probe technique. In Section 3 spectral analysis techniques are described, in particular higher-order spectral analysis and spectral transfer. Section 4 illustrates application of the spectral transfer analysis to experimental results from the H-1 heliac. Experimental evidence of the inverse energy cascade is presented. In Section 5 we describe a model experiment in two-dimensional fluid turbulence to compare physics of the inverse energy cascade and generation of large coherent structures in fluids with generation of zonal flows in plasma turbulence. Experimentally identifiable signatures of zonal flows in plasma are also illustrated.

Michael Shats and Hua Xia

#### 236

# 5.2. Experimental techniques and diagnostic tools in plasma turbulence

Main difficulties in experimental studies of turbulence are related to:

- (1) usual problems in understanding turbulence in any medium;
- (2) limited accessibility due to the high temperature and high vacuum conditions, intense fluxes of particles and heat from the plasma:
- (3) difficulties in interpretation of measurements which are typically limited to just a few spatial locations;
- (4) difficulty of imaging and visualization of turbulent fields in fully ionized plasma;
- (5) the multi-field nature of the plasma turbulence: simultaneous presence of fluctuations in the density, temperature, electric fields, magnetic fields, etc.

Plasma turbulence has been studied using a variety of tools and techniques. One can adopt several ways of classifying the plasma fluctuation diagnostics. For example, they can be classified according to the measured plasma parameters, such as the fluctuations in the electron density, electrostatic potential, electron temperature, magnetic field, etc. Turbulence diagnostics can also be viewed according to the physical principles used for the measurements, such as the refractive index measurements, scattering of the electromagnetic radiation, measurements of the plasma particle fluxes and others.

In this section we do not overview plasma turbulence diagnostics. There are several good review papers, which cover diagnostics used in plasma turbulence studies, such as.<sup>20,21</sup> For the state-of-the-art methods in plasma diagnostics, including the turbulence measurements, one should consult Proceedings of the Topical Conferences on High-Temperature Plasma Diagnostics held bi-annually. The latest Proceedings have been published in *Reviews of Scientific Instruments*, Volume 75, Issue 10, 2004. Here we briefly describe selected experimental techniques which have been particularly successful in characterizing key plasma turbulence phenomena in the last 15-20 years.

# 5.2.1. Langmuir probes

Langmuir probes<sup>22,23</sup> are probably the most basic tools for the plasma turbulence studies. They are relatively easy to design, and they have excellent spatial resolution which is determined by the size of the probe tip and by the accuracy of its positioning within the plasma. However they have a somewhat limited applicability in toroidal plasma experiments since they

cannot withstand very high fluxes of particles and energy. As a result, their applications are limited to either the peripheral plasma in large high-temperature experiments, or to the low-temperature plasma in the smaller-scale laboratory experiments, such as for example, the H-1 heliac.

Langmuir probes provide measurements of the electron density,  $n_e$ , electrostatic potential,  $\phi$ , the electron temperature,  $T_e$  and their fluctuations,  $\tilde{n}_e$ ,  $\tilde{\phi}$ , and  $\tilde{T}_e$ . When several probe tips are mounted on the same probe shaft, Langmuir probes can be used to measure the fluctuation wave numbers and various components of the turbulent electric fields.

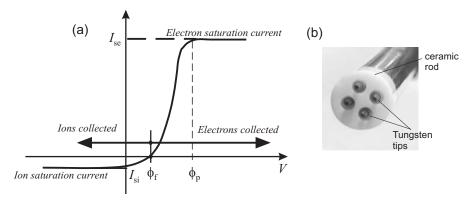


Fig. 5.1. (a) Current-voltage characteristic of the Langmuir probe in plasma. (b) Design of the 4-pin Langmuir probe

The current-voltage characteristic of a Langmuir probe in the plasma is shown in Fig. 5.1.(a). The potential at the probe corresponding to the zero current is referred to as the *floating potential*,  $\phi_f$ . A Langmuir probe will draw an electron current, I, when biased to a voltage  $V > \phi_f$ . When the probe is biased at  $V < \phi_f$ , it collects ions. At sufficiently high negative bias, the current to the probe saturates at the level of the *ion saturation current*:

$$I_{si} = e^{-1/2} q A_p n_e c_s, (5.1)$$

where

$$c_s = \sqrt{\frac{q(ZT_e + T_i)}{m_i}}. (5.2)$$

is the ion acoustic velocity,  $T_e$  and  $T_i$  are the electron and ion temperatures respectively,  $A_p$  is the probe collecting area,  $m_i$  is the ion mass, and Z is the ion charge state.

At sufficiently high positive bias voltage, the electron probe current saturates at the level of the *electron saturation current*,

$$I_{se} = \frac{1}{4} q A_p n_e V_{te}, (5.3)$$

where

$$V_{te} = \sqrt{\frac{8qT_e}{\pi m_e}}. (5.4)$$

is the electron thermal velocity. The positive bias potential  $\phi_p$ , corresponding the the electron saturation current, is referred to as the *plasma potential*. For  $V < \phi_p$ , the probe current can be expressed as<sup>22</sup>

$$I = I_{se} \exp\left(\frac{V - \phi_p}{T_e}\right) - I_{si}. \tag{5.5}$$

The electron temperature  $T_e$  can be determined from the slope of a semilog plot of I versus V. This slope is equal to  $e/kT_e$  in the electron-retarding region  $(V < \phi_p)$ .

Thus several basic plasma parameters and their fluctuations can be deduced from the probe I-V characteristic if the bias voltage is swept sufficiently fast. In some cases, the sweep frequency may limit the time resolution of the probe measurements.

An alternative solution may be in using a probe which has several tips biased at different potentials. Such a probe design is illustrated in Fig. 5.1.(b). This an extension of the principle of the triple probe.<sup>24</sup> Triple probes allow instantaneous values of the electron temperature  $T_e$ , as well as the electron density to be determined. The electron temperature can be derived by continuously sampling two points on the characteristic, the floating potential,  $\phi_f$ , and a positive potential,  $\phi_+$ , corresponding to a current which is equal to  $I_{si}$  but is oppositely directed. In this case the electron temperature can be determined as<sup>24</sup>

$$T_e = \frac{(\phi_+ - \phi_f)}{\ln 2}. (5.6)$$

The plasma potential can also be determined from the triple probe  $as^{23}$ 

$$\phi_p = \phi_f + \alpha T_e, \tag{5.7}$$

where

$$\alpha = -\frac{1}{2} \ln \left( 2\pi \frac{m_e}{m_i} \left( 1 + \frac{T_i}{T_e} \right) (1 - \delta)^{-2} \right),$$
 (5.8)

and  $\delta$  is the secondary electron emission coefficient.

The ability of the triple probe to simultaneously measure fluctuations in the floating potential and in the electron temperature is particularly valuable in the turbulence studies. As will be shown below, fluctuations in the plasma potential is one of the key parameters which determine the turbulence-driven transport. The plasma potential can be deduced from the triple probe data using Eq. (5.7). Also, the time-resolved measurements of  $T_e$  allow time-varying electron density  $n_e$  to be derived from the measurements of the ion saturation current  $I_{si}$ , Eq. (5.1).

### 5.2.2. Characterization of turbulent transport using probes

Langmuir probes can be arranged in arrays to characterize plasma turbulence. In this subsection we consider measurements of the turbulence-driven fluxes using Langmuir probes. We limit our discussion to the measurements of the particle fluxes due to electrostatic fluctuations. The particle flux measurements are crucial for understanding the roles of turbulence in the plasma confinement and require simultaneous characterization of the fluctuations in the radial velocity of particles and the density fluctuations. The Langmuir probe array is the only diagnostic capable of performing such measurements with required spatial and temporal resolution.

In case of the electrostatic turbulence (e.g., drift-wave turbulence, see Chapter 4 by J. Krommes) electrons and ions fluctuate in the radial direction due to the  $E \times B$  drift in the fluctuating poloidal electric field,  $\widetilde{E}_{\theta}$ ,

$$\widetilde{v}_{rad} = \frac{\widetilde{E}_{\theta}}{B} = \frac{k_{\theta}\widetilde{\phi}}{B}.$$
(5.9)

The fluctuation-driven flux is then

$$\widetilde{\Gamma}_{fl} = \frac{\widetilde{n}\widetilde{E}_{\theta}}{B} = \frac{k_{\theta}}{B} \left( \widetilde{n}\widetilde{\phi} \right). \tag{5.10}$$

The time-average fluctuation-driven particle flux can also be defined in the frequency domain as:  $^{25}$ 

$$\Gamma_{fl} = \frac{2}{B} \int_{0}^{\infty} d\omega \left[ P_{nn} P_{EE} \right]^{1/2} |\gamma_{nE}| \cos \left[ \alpha_{nE} \right], \tag{5.11}$$

where  $P_{nn}$  and  $P_{EE}$  are the spectral power densities of the fluctuations in the electron density and poloidal electric field. The coherence  $0 \le |\gamma_{nE}| \le 1$  is defined *via* the cross- and auto-power spectra of the fluctuations as

$$\gamma_{nE}(\omega_k) = \left(\frac{\left[Re\left(P_{nE}(\omega_k)\right)\right]^2 + \left[Im\left(P_{nE}(\omega_k)\right)\right]^2}{P_{nn}(\omega_k)P_{EE}(\omega_k)}\right)^{1/2},\tag{5.12}$$

Michael Shats and Hua Xia

240

while  $\alpha_{nE}$  is the phase shift between  $\tilde{n}$  and  $\tilde{E}_{\theta}$ :

$$\alpha_{nE}(\omega_k) = \arctan\left(\frac{Im\left(P_{nE}(\omega_k)\right)}{Re\left(P_{nE}(\omega_k)\right)}\right).$$
 (5.13)

Here Im and Re denote the imaginary and the real parts of the cross-spectra.

Eq. (5.11) shows that the particle flux can be reduced either by suppressing the turbulence  $(P_{nn} \text{ and } P_{EE} \text{ reduction})$ , or by decorrelating density and  $E_{\theta}$  fluctuations  $(\gamma_{nE} \to 0)$ , or by changing the relative phase  $\alpha_{nE}$  between them. Depending on the phase shift  $\alpha_{\tilde{n}\tilde{E}}$  between  $\tilde{n}$  and  $\tilde{E}_{\theta}$ , the time-average flux can be zero  $(\alpha_{\tilde{n}\tilde{E}} = \pi/2)$ , positive (radially outward), or negative (radially inward). Below we will illustrate that all these parameters affect turbulent particle fluxes in magnetized plasma.

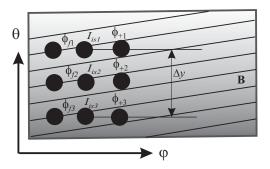


Fig. 5.2. Example of the probe array suitable for the characterization of the turbulence-driven particle flux.

Figure 5.2. shows the geometry of the Langmuir probe array capable of measuring the fluctuation-driven flux. Three triple probes,  $(I_{is1}, \phi_{f1}, \phi_{+1})$ ,  $(I_{is2}, \phi_{f2}, \phi_{+2})$ , and  $(I_{is3}, \phi_{f3}, \phi_{+3})$  measure the electron temperature and the plasma potentials at three poloidally shifted locations in the plasma. Since fluctuations in toroidal plasma are strongly elongated in toroidal direction (toroidal wave numbers,  $k_{\varphi}$ , are much smaller than either poloidal  $k_{\theta}$ , or radial  $k_r$  wave numbers), a small relative shift of the triple probe tips in toroidal direction does not affect phases of the fluctuations. Probes 1 and 3 give  $\phi_{p1}$  and  $\phi_{p3}$  using Eq. (5.7), such that the fluctuations in the poloidal electric field can be computed as  $\widetilde{E}_{\theta} = (\widetilde{\phi}_{p1} - \widetilde{\phi}_{p2})/(\Delta y)$ . This  $\widetilde{E}_{\theta}$  is multiplied with the fluctuations in the electron density to obtain  $\widetilde{\Gamma}_{fl}$  using Eq. (5.10) or Eq. (5.11).  $\widetilde{n}$  is deduced from the ion saturation current of the probe 2 using Eq. (5.1) and  $T_{e2}$ .

In practice, in many experiments floating potentials are often used instead of the plasma potentials. This can only be justified when  $\widetilde{\phi}_f$  and  $\widetilde{T}_e$  are in phase, which needs to be proven experimentally. If this is the case, the probe array can be greatly simplified.

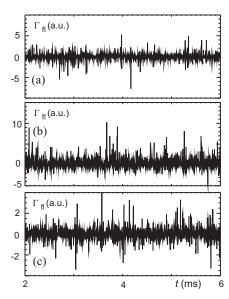


Fig. 5.3. Time-resolved fluctuation-driven flux,  $\Gamma_{fl} = \tilde{n} \ \tilde{E}_{\theta} \ / \ B$ 

An example of the experimentally measured time-resolved fluctuation-driven flux is shown in Fig. 5.3.. It is seen that  $\Gamma_{fl}$  has a bursty structure, such that it is the statistics of positive and negative bursts which determines the direction of the time-average flux. Three plots in Fig. 5.3. correspond to the inward (a), outward (b), and zero-average flux (c).

So far we have assumed that the particle fluxes driven by the turbulent fluctuations are the same for electrons and ions, in other words,  $\Gamma$   $_{fl}^{e} = \Gamma$   $_{fl}^{i}$ . There are however several physics effects which can break this balance. It has been mentioned in the Introduction that turbulence can drive plasma flows, such as, for example, zonal flow. The Reynolds stress is an example of such a mechanism. Turbulence induced Reynolds stress drives the plasma flow which can be associated with the radial current:<sup>26</sup>

$$J_r = \frac{m_i n_e}{eB} \frac{\partial}{\partial r} \left\langle \widetilde{v}_{ri} \widetilde{v}_{\theta i} \right\rangle. \tag{5.14}$$

Another example is the flow driven due to the finite-Larmor-radius

(FLR) effect.  $^{27,28}$  In any case such flow generation would be manifested as the fluctuation-driven radial current

$$J_r = e\left(\left\langle \widetilde{n}_i \widetilde{V}_{ri} \right\rangle - \left\langle \widetilde{n}_e \widetilde{V}_{re} \right\rangle \right), \tag{5.15}$$

which can change the radial electric field and generate plasma flow in either poloidal or toroidal direction.

The first experimental evidence of the fluctuation-driven radial electric current has been found in the H-1 heliac.<sup>29</sup> Fluctuations in the ion radial velocity were measured using the so-called Mach (or paddle) probe. Such probes are used to provide information about plasma flow velocities.<sup>30</sup> A Mach probe typically consists of two identical collectors separated by an insulator. Both collectors are negatively biased into the ion saturation current. According to Eq. (5.1) the ion saturation current is dependent on the velocity at which the ions stream towards the probe. Therefore, if the plasma drifts with some velocity perpendicular to the axis of the probe, the two probe tips will collect ions arriving with different velocities and therefore measure different currents.

If the ion gyroradius is larger than the probe size, then such a probe is referred to as "unmagnetized". A revision of the Bohm theory suitable for the unmagnetized Mach probe has been presented in. Since the Mach probe is unmagnetized, it can be oriented to be sensitive to the ion radial velocity and its fluctuations  $\tilde{V}_{ri}$ . This provides an independent estimate for the ion fluctuation-driven flux  $\Gamma_i = \left\langle \tilde{n}_i \tilde{V}_{ri} \right\rangle$ . The fluctuation-induced flux for the electrons was assumed a result solely of  $\tilde{E} \times B$ , where the main contribution comes from the poloidal  $\tilde{E}$  component  $(\tilde{E}_{\theta})$  and the toroidal B component  $(B_t)$ . It was found that the fluctuations in the ion radial velocity are significantly lower than those for electrons. As a result the fluctuation-driven fluxes are different for electrons and ions, which leads to the production of a radial current.

# 5.2.3. Collective (Bragg) scattering of electromagnetic waves by density fluctuations

Experimental results obtained using collective scattering diagnostic have greatly influenced studies of turbulence in 1970s and 1980s. The most important result is that the wave number spectra of the plasma turbulence are broad and have maximum at rather low wave numbers. Collective, or Bragg scattering diagnostic is capable of directly measuring the wave number spectra of the density fluctuations in plasma.

The process of scattering of electromagnetic waves in plasma can be

thought of as follows. The incident electromagnetic wave impinges on plasma particles. Particles are accelerated in the wave. Accelerated particles emit electromagnetic radiation in all directions. This emitted radiation is the scattered wave.

Whether the wave is scattered by electrons participating in collective motion, or by the unshielded electrons, is determined by the scattering parameter  $\alpha$ :

$$\alpha = \frac{1}{k\lambda_D},\tag{5.16}$$

where  $\lambda_D$  is the Debye length and k is the wave number of the plasma density fluctuations. When  $\alpha \geq 1$ , the main contribution to the scattered wave comes from oscillations of wavelength longer than the Debye length. This is called the *collective domain*. In the process of scattering the incident electromagnetic wave  $(\mathbf{k}_0, \omega_0)$  interacts with the plasma wave  $(\mathbf{k}, \omega)$  such that the scattered wave  $(\mathbf{k}_s, \omega_s)$  is generated. The momentum and energy are conserved in each act of scattering:

$$\mathbf{k} = \mathbf{k_s} - \mathbf{k_0}, \ \omega = \omega_s - \omega_0, \tag{5.17}$$

The wave vector diagram illustrating this is shown in Fig. 5.4.. The angle,  $\theta$  between the wave vectors of the incident and the scattered waves is called the scattering angle. By selecting different scattering angles, scattering by different wave lengths in the plasma can be studied. The relation between the scattering angle and the fluctuation wave vector k is given by the Bragg rule:

$$k = 2k_0 \sin \theta / 2,\tag{5.18}$$

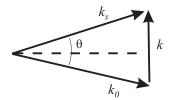


Fig. 5.4. Wave vectors of the waves participating in Bragg scattering

The Bragg rule follows from the fact that the wave vector triangle in Fig. 5.4. is isosceles because

$$\omega_0 \approx \omega_s >> \omega, \ k_s = \frac{\omega_s}{c} = \frac{\omega + \omega_0}{c} \approx k_0 = \frac{\omega_0}{c}.$$
 (5.19)

An example of the microwave scattering geometry is shown in Fig. 5.5.. Detailed description of this diagnostic can be found in.<sup>32</sup> The microwave beam at the wavelength of  $\lambda_0 \approx 2$  mm is focused into the plasma using the horn-mirror antenna. This radiation, scattered at four different angles in the plasma, is collected using four similar receiving antennas. It should be noted that the size of the scattering volume is determined by the intersection of the radiation patterns of the incident and the receiving antennas. This volume is larger for the smaller scattering angles (longer wave length of the plasma fluctuations). The larger the scattering angle, the better the spatial resolution of the diagnostic.

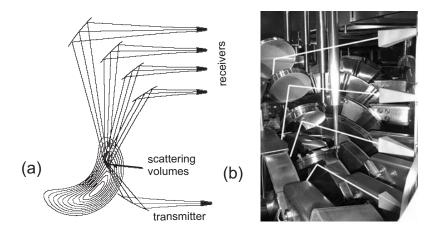


Fig. 5.5. (a) Schematic of the microwave scattering diagnostic in the H-1 heliac. (b) Photograph of the receiving microwave mirror-horn antennas installed inside the H-1 vacuum tank.

As seen from Eq. (5.18), for a given wave number of the density fluctuation, the scattering angle becomes very small if lasers are used instead of the microwave sources. For example, to detect fluctuations having  $\lambda=2$  mm one needs to collect the microwave beam at  $\lambda_0=2$  mm scattered at  $\theta=60$  degrees. If one uses a  $CO_2$  laser at  $\lambda_0=10.6~\mu m$ , the scattering angle should be  $\theta\approx0.3$  degrees, or 2.66 mrad. For such small scattering angles the size of the scattering volume extends beyond the diameter of the plasma cross-section, such that the spatial resolution becomes poor. In this case other techniques, such as the crossed laser beams are used. For details see, for example.<sup>3</sup>

Scattered radiation is then analyzed, and if the heterodyne detection scheme is used,<sup>32</sup> the direction of the propagating density waves can be determined in addition to their amplitude and the frequency spectra.

# 5.2.4. Reflectometry in fluctuation studies

Reflectometry has been widely used for measuring density fluctuations in the high temperature plasma. Measurements rely on the existence in the plasma of the cut-off layer, at which the refractive index for the probing electromagnetic wave is zero. For example, for the ordinary electromagnetic wave in plasma (a wave whose electric field vector  $\boldsymbol{E}$  is parallel to the local vector of the magnetic field  $\boldsymbol{B}$ )

$$N^2 = 1 - \frac{\omega_{pe}^2}{\omega^2} = 0. {(5.20)}$$

Here  $\omega_{pe}$  is the electron plasma frequency, and  $\omega$  is the frequency of the probing electromagnetic wave. The critical density, at which the wave is reflected at the cut-off layer is given by

$$n_c = \frac{m_e \epsilon_0 \omega^2}{e^2}. (5.21)$$

The phase difference between the incident and reflected waves is sensitive to the position of the cut-off layer. Since in the presence of turbulence the layer of the critical density fluctuates, measurements of the phase and of the amplitude of the reflected wave can, in principle, give information about local fluctuations at the cut-off layer. A great advantage of the reflectometers is a relatively easy access to the plasma since both the incident and the reflected beams are transmitted through the same vacuum window. Reflectometers allow radial scans of the cut-off layer by sweeping the microwave frequency. They possess good spatial resolution since the cut-off layer is very thin.

The schematic of a reflectometer is shown in Fig. 5.6.. This is an example of the heterodyne detection scheme in which the reflected wave at the frequency  $f_0 + \Delta f$  is mixed with the wave of the local oscillator (LO) to produce a signal at the intermediate frequency,  $f_0 - f_{LO} + \Delta f$ , which is then processed in the quadratic (IQ) detector to produce two low-frequency output signals proportional to the sine and cosine of the phase. The reflected wave is characterized by its amplitude, A, and the phase,  $\varphi$ .

If the reflected wave is coherent, strong phase fluctuations are usually measured, while the fluctuations in the amplitude are weak. However, in many experimental situations the reflected wave is incoherent, such that its phase is randomly distributed around zero. In this case the interpretation of the reflectometer data is not straightforward and requires additional modelling.

Main reasons for difficulties in the interpretation of the reflectometer signals are as follows:

• "Rigid" motion of the cutoff surface changes the path length x (see Fig. 5.6.) which affects the phase  $\varphi$  of the reflected wave;

Michael Shats and Hua Xia



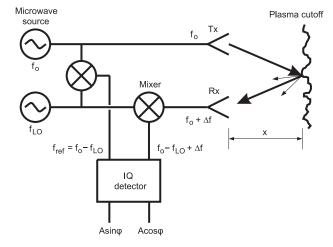


Fig. 5.6. Schematic of the microwave reflectometer. Figure courtesy G.D. Conway.

- Bragg back scattering, or the scattering at  $\theta = 180$  degrees contributes to reflected wave. In this case fluctuations in the cut-off layer, whose wave number satisfy  $k = 2k_0$  (see Eq. 5.18), "pollute" the reflected signal.
- The interference in reflected microwaves may be caused by "roughness" of the reflection surface when  $k \perp \nabla n_e$  or  $k \perp B$ .

For details on the problems with the interpretation of the reflectometer data and ways of solving it see references  $^{33-36}$  which describe various models used in the interpretation of measurements ("random phase screen", "distorted mirror" etc.).

#### 5.2.5. Doppler reflectometry

The Doppler reflectometer can be considered as a hybrid between a reflectometer and collective scattering diagnostic. <sup>17,37</sup> The schematic of the Doppler reflectometer is shown in Fig. 5.7.. The experimental setup consists of the microwave reflectometer with antennas poloidally tilted to deliberately misalign the angle  $\theta$  between the incident beam and the normal to the plasma cut-off layer. The diagnostic is sensitive to the perpendicular density fluctuation having a wave number determined by the Bragg rule (Eq. (5.18)),  $k_{\perp} = 2k_0 \sin \theta/2$ .

Poloidal motion of the density turbulence at the cutoff layer induces a Doppler frequency shift  $f_D$  in the reflected signal. This frequency shift

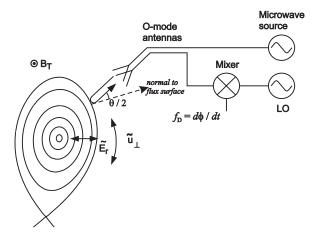


Fig. 5.7. Schematic of the Doppler reflectometer. Figure courtesy G.D. Conway.

is proportional to the perpendicular rotation velocity of turbulence,  $u_{\perp} = V_{E \times B} + V_{phase}$  ( $V_{phase}$  is the phase velocity of turbulent fluctuation in the plasma frame of reference):

$$f_D = \frac{u_{\perp} k_{\perp}}{2\pi} = \frac{u_{\perp} 2 \sin \theta / 2}{\lambda_0}.$$
 (5.22)

By changing the tilt angle  $\theta$  and by measuring the received power, a perpendicular wave number spectrum  $S(k_{\perp})$  can be obtained.

In many experimental situations the Doppler shift due to the  $E \times B$  drift dominates over the phase velocity in the plasma frame,  $V_{E \times B} >> V_{phase}$ . As a result, the frequency shift,  $f_D$ , will be proportional to the radial electric field,  $E_r$ . Radial electric field fluctuations  $\tilde{E}_r$  will appear in  $f_D$  and can be detected as a spectrally broadened feature around  $f_D$  in the scattered wave spectrum. This technique has been successfully used to detect low-frequency oscillations in  $E_r$  due to the presence of the geodesic acoustic mode.<sup>17</sup>

# 5.2.6. Optical imaging of turbulent fluctuations

The spectral line radiation emitted by excited neutrals and ions contains useful information about plasma parameters, such as the electron temperature and density. However, in the high-temperature interior of the fusion-relevant plasma, atoms are fully ionized, such that only the impurity radiation can be measured for the diagnostic purposes.

When the neutral beam is injected into the plasma, the beam atoms become collisionally excited and radiate. This radiation due to the interaction of the beam particles with electrons and ions is used to derive local density and its fluctuations in the diagnostic method referred to as the beam emission spectroscopy (BES). $^{38,39}$ 

Figure 5.8. shows experimental setup of the BES diagnostic on the DIII-D tokamak. A beam of deuterium atoms having energy of  $E=75~\rm keV$  is launched tangentially into the plasma. Such a high energy of the beam atoms leads to a Doppler shift in the wave length of the radiated emission. This can be used to distinguish the radiation emitted by the beam particles from the neutral emission originated at the plasma edge. The light is collected along several chords perpendicular to the neutral beam. In this example a matrix of  $4\times 4$  optical fibres is imaged into the plasma such that the light in each of the optical channels comes from a small volume in the plasma determined by the intersection between the neutral beam and the fibre image in the plasma. Spatial resolution also depends on the radiative lifetime,  $\tau$ , of a chosen excited state. This should be small  $(10^{-9} - 10^{-8} {\rm s})$  because spatial resolution is proportional to the square root of the beam energy (velocity) and the lifetime:  $l \propto \sqrt{E}\tau$ .

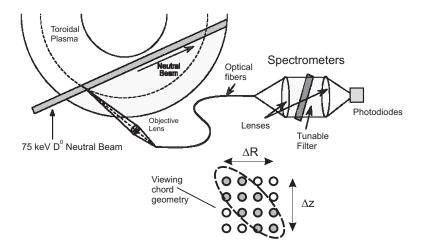


Fig. 5.8. Setup of the beam emission spectroscopy on the DIII-D tokamak. Figure courtesy G. McKee

The relative level of the local density fluctuations in each of the intersection volumes is proportional to the relative level of the fluctuations in the intensity of the light emission I:

$$\frac{\tilde{n}}{n} = K(T_e, n_e) \frac{\tilde{I}}{I},\tag{5.23}$$

where the proportionality constant K is determined by the atomic physics relevant to the excitation of a given spectral line and depends on the electron temperature and density.

Though the line emissivity is proportional to the electron density, fluctuating velocity field can also be obtained from the measured fluctuating density. In this case two-dimensional cross-correlation analysis of the  $\tilde{n}$ -field is used. This method has been successful in identifying radially sheared zonal flows in the DIII-D tokamak.<sup>13</sup>

# 5.2.7. Heavy ion beam probe

Measurements of the electrostatic potential fluctuations is one of the most challenging problems in experimental plasma turbulence studies. With the exception of the Langmuir probes, whose operational range is limited to the cold edge plasma, the *heavy ion beam probe* (HIBP) is the only diagnostic capable of providing information about the electrostatic potential from the plasma core. $^{40,41}$ 

The principle of the diagnostic is as follows. A beam of heavy ions (e.g. gold, caesium, or thallium) of very high energy (hundreds of keV) is launched into the magnetized plasma. High energy and large mass of ions are needed to increase the ion gyroradius,  $\rho_i = (m_i v_{i\perp})/qB$  (where  $m_i$  is the ion mass,  $v_{i\perp}$  is the component of the ion velocity perpendicular to the magnetic field B, and q is the ion charge). In this case  $\rho_i$  exceeds the diameter of the plasma column and ions will not be confined by the magnetic field. As the incident ion beam propagates through the plasma, the probe ions are ionized through the electron impact collisions. As a result, their charge increases and the trajectories of these secondary ions deviate from the trajectory of the primary ion beam as shown in Fig. 5.9.. A small fraction of the primary beam ions enters the detector. The energy of the secondary ions originated in a small sample volume (determined by the intersection of trajectories of primary and secondary ions) is then analyzed. Their energy exceeds the energy of the primary ions by the amount equal to the electric potential in the sample volume. The intensity of the secondary beam reflects the electron density in sample volume. The intensity S of the secondary beam is given by:<sup>16</sup>

$$S = \sigma n_e(r)(\delta r)e^{-\int \sigma n_e dl}I_0, \qquad (5.24)$$

where  $I_0$  is the injected beam current,  $\sigma$  is the ionization cross-section by electron impact,  $\delta l$  is the length of the sample volume determined by the width of the detector aperture. The integral extends along the beam trajectory. The position of the sample volume can be swept through plasma by changing the direction and energy of the primary beam.

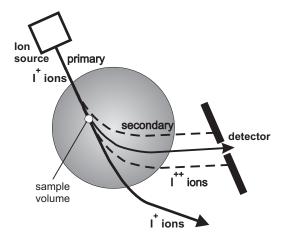


Fig. 5.9. Schematic of the heavy ion beam diagnostic.

Fluctuations in the observed energy and intensity of the secondary ion beam are proportional to fluctuations in electrostatic potential and electron density respectively. The HIBP diagnostic has become a powerful tool capable of providing valuable information on the low-frequency potential fluctuations from the inner plasma regions in tokamaks and stellarators (see, for example, <sup>15,16</sup>).

# 5.3. Spectral analysis techniques

In this section spectral analysis techniques used in experimental turbulence studies are overviewed. Turbulence, which to large extent determines the plasma behaviour, is characterized by broad wave number spectra whose maxima are observed at the longest measured scales.<sup>3</sup> Since unstable waves, which generate turbulence are initially unstable only in a limited spectral range, mechanisms of the nonlinear wave-wave interaction are needed to explain observations.

For example, three-wave interactions may lead to the energy cascade which spreads spectral energy over the spectrum. In two-dimensional (2D)

turbulence<sup>42</sup> (see Chapter 1) and in magnetized plasma<sup>9</sup> spectral energy is transferred to lower wave numbers (larger scales) in the process of the so-called inverse energy cascade. If the energy dissipation at large scales is low, spectral energy can condense in large coherent structures, such as, for example, vortex structures (for review see<sup>43</sup>) and zonal flows.<sup>44</sup>

Signatures of nonlinear interactions in broad spectra can be revealed by analysing the higher order moments of the turbulence spectra. The presence of the three-wave interactions can be detected using a *bispectrum*. Four-wave interactions can be revealed by means of a *trispectrum*.

Bispectra, which measure the amount of the phase correlation between three spectral components, have been used in plasma research for a long time.  $^{45-47}$  Other higher order spectral characteristics, such as the bicoherence (normalized bispectrum), trispectrum,  $^{48,49}$  etc., have been developed in recent years.

The higher order spectral analysis does not determine however the direction of the energy transfer. The nature and the direction of the spectral transfer have direct impact on the way in which the instability-driven turbulence is saturated, on the magnitude and shape of the spectrum, and ultimately on the nature of the particle and energy transport produced by turbulence.

A method of computing the power transfer function (PTF) was developed and applied to the fluid and plasma turbulence in 1980s. The method allows quantitative estimates of the nonlinear coupling coefficients and the energy cascades from experimentally measured turbulent signals to be made.  $^{50,51}$  In the PTF technique, linear and quadratic transfer functions are estimated from the measured fluctuation signals x(s) and y(s) in either temporal, or in spatial domain. Spectral transfer is described by the wave coupling equation which is appropriate in a single-field turbulence. The PTF method is based on the quantitative description of nonlinear interactions between different scales using statistically averaged estimation of the power spectra, bispectra and other higher order moments.

The technique was first applied to experimental data in the nonlinear stages of a transition flow of a wake behind a thin flat plate.  $^{52}$  Later this technique was applied to the turbulence measured at the edge plasma of the Texas Experimental Tokamak.  $^{51}$ 

A modified version of the PTF technique was proposed in.<sup>53</sup> In the modified method, non-ideal spectra which do not participate in the three-wave interactions are taken into account. The method was tested using simulated 1D turbulence data generated using the Hasegawa-Mima model and 2D data using the Terry-Horton model. Both of these are the single-field models. The modified technique was able to accurately reproduce the input characteristics (the linear growth rate and nonlinear energy transfer)

of the simulated data.

In this section we will overview the higher order spectral analysis (HOSA) techniques, and then will describe the PTF technique. The amplitude correlation method is another technique suitable for studying energy transfer between different spectral regions. The amplitude correlation technique complements the PTF analysis in situations where the coherent phase interactions dominates over the random-phase interactions.

### 5.3.1. Higher-order spectral analysis

The presence of three-wave interactions in turbulence can be detected by means of a bispectrum. $^{45}$  The auto-bispectrum of a signal is defined as:

$$B(f_1, f_2) = \langle X_f X_{f_1}^* X_{f_2}^* \rangle, \qquad f = f_1 + f_2,$$
 (5.25)

where  $X_f$  is a Fourier transform of the signal under investigation and \*denotes the complex conjugate.

Auto-bispectra measure the statistical relationship between spectral components at the frequencies  $f_1$ ,  $f_2$  and  $f = f_1 + f_2$ .

If the Fourier transform of the signal is  $X_f = A_f e^{\phi_f}$ , the auto-bispectrum of the signal can then be expressed as:

$$B(f_1, f_2) = \langle A_{f_1} A_{f_2} A_f e^{(\phi_f - \phi_{f_1} - \phi_{f_2})} \rangle, \qquad f = f_1 + f_2 . \tag{5.26}$$

If waves at  $f_1$ ,  $f_2$  and f have statistically independent random phases (like in a Gaussian signal), the resulting biphase  $\phi = \phi_f - \phi_{f_1} - \phi_{f_2}$  of the polar representation (Eq. (5.26)) will be random and the averaged value of the bispectrum will be zero. If, however, a coherent phase relationship exists due to the nonlinear coupling between these waves, the auto-bispectra (averaged over many realizations) will have a finite value.

A similar definition can be given to a bispectrum between two signals, x(t) whose Fourier transform is  $X_f$  and y(t) whose Fourier transfer is  $Y_f$ . A cross-bispectrum is a useful characteristic of three-wave coupling effects between two turbulent spectra.

$$B(f_1, f_2) = \langle Y_f X_{f_1}^* X_{f_2}^* \rangle \qquad f = f_1 + f_2 . \tag{5.27}$$

A nonzero bispectrum is indicative of either (1) strong three-wave interactions or (2) weak interactions between spectral components having large amplitudes, as can be seen from the definition of the bispectrum, Eq. (5.26). To avoid this ambiguity, the *bicoherence*, which is the bispectrum normalized by the amplitude of the interacting waves can be used to accentuate the strength of the three-wave interactions:

$$Bic^{2}(f_{1}, f_{2}) = \frac{|\langle Y_{f} X_{f_{1}}^{*} X_{f_{2}}^{*} \rangle|^{2}}{\langle Y_{f} Y_{f}^{*} \rangle \langle X_{f_{1}} X_{f_{1}}^{*} \rangle \langle X_{f_{2}} X_{f_{2}}^{*} \rangle}, \quad f = f_{1} + f_{2}$$
 (5.28)

The value of the bicoherence varies between 0 and 1, similarly to the usual 1st order coherency given by Eq. (5.12).

# 5.3.2. Wave coupling equation

The wave coupling equation which describes the time evolution of the spectral components in the turbulence spectra lies in the heart of the spectral transfer analysis. This equation has already been introduced in Chapter 1 (Eq. (5)) as a kinetic wave equation and in Chapter 4 (Eq. (96)) during the discussion of the weak-turbulence theory.

The wave coupling equation can be expressed as follows:

$$\frac{\partial \phi(k,t)}{\partial t} = (\gamma_k + i\bar{\omega}_k)\phi(k,t) + \frac{1}{2} \sum_{\substack{k_1,k_2,\\k=k_1+k_2}} \Lambda_k^Q(k_1,k_2)\phi(k_1,t)\phi(k_2,t), \quad (5.29)$$

where  $\psi(x,t)$  is the fluctuation field,  $\phi(k,t)$  is the spatial Fourier spectrum of the fluctuation field  $\psi(x,t) = \sum_k \phi(k,t) e^{ikx}$ .

The wave coupling equation describes the rate of change of the spectral components due to linear and nonlinear effects, namely, due to the mode growth at the rate  $\gamma_k$ , its dispersion  $\bar{\omega}_k$ , and due to the wave-wave coupling. The coupling coefficient  $\Lambda_k^Q(k_1, k_2)$  represents the strength of the wave coupling. A wave  $(k, \omega)$  thus decays into two waves  $(k_1, \omega_1)$  and  $(k_2, \omega_2)$  or two waves merge into one.

This equation describes the wave coupling in the weak-turbulence theory in the random-phase approximation, but a similar equation can be derived from a more specific models, such as the Hasegawa-Mima model (see Section 1.4 of Chapter 4). Equation (5.29) can also be constructed on purely phenomenological grounds using a black-box approach as will be discussed in the next subsection. It should also be noted that to analyze the spectral transfer in plasma turbulence using the wave kinetic equation one needs to justify the validity of the single field description of turbulence. Such description is not always valid, however it is possible in several important models (e.g. in the Hasegawa-Mima model) and in some experiments, as will be discussed below.

The Hasegawa-Mima equation is the basis of the simple drift wave model.  $^{8,54}$ 

$$\frac{\partial}{\partial t} (\nabla^2 \phi - \phi) - [(\nabla \phi \times \hat{z}) \cdot \nabla] \left[ \nabla^2 \phi - \ln \left( \frac{n_0}{\omega_{ci}} \right) \right] = 0.$$
 (5.30)

If we expand  $\phi(x,t)$  in a spatial Fourier series, as

$$\phi(x,t) = \frac{1}{2} \sum_{k} (\phi_k(t)e^{ik \cdot x} + c.c), \tag{5.31}$$

Michael Shats and Hua Xia

254

where k is  $k_{\perp}$ , Eq. (5.30) is reduced to

$$\frac{\partial \phi(k,t)}{\partial t} + i\omega_k^* \phi_k(t) = \frac{1}{2} \sum_{\substack{k_1,k_2\\k=k_1+k_2}} \Lambda_k(k_1,k_2) \phi(k_1,t) \phi(k_2,t).$$
 (5.32)

Here, the matrix element  $\Lambda_{k_1,k_2}$  is given by

$$\Lambda_{k_1,k_2} = \frac{1}{1+k^2} (k_1 \times k_2) \cdot \hat{z}[k_2^2 - k_1^2]. \tag{5.33}$$

 $\omega_k^*$  is the normalized (by  $\omega_{ci}$ ) drift wave frequency given by

$$\omega_{ci}^* = \frac{-k_\theta T_e \partial(\ln n_0)/\partial r}{eB_0(1+k^2)\omega_{ci}}.$$
 (5.34)

Equation (5.32) is the Hasegawa-Mima equation in the Fourier space. It contains the mode coupling of different modes of fluctuations and the linear dispersion of the modes, and it has exactly the same form as the wave coupling equation, Eq. (5.29).

As explained in Chapter 4 (section 1.4.1), when the background density gradient and the adiabatic electron response are neglected, the Hasegawa-Mima equation, Eq. (5.30), closely resembles the equation for the stream function  $\psi$ , which can be derived from the 2D Euler equation for the vorticity:

$$\frac{\partial}{\partial t} \nabla^2 \psi - [(\nabla \psi \times \hat{z}) \cdot \nabla] \nabla^2 \psi = 0. \tag{5.35}$$

The Fourier-transform of the 2D Euler equation for the streamfunction takes a form which is very similar to the wave coupling equation, Eq. (5.29).<sup>8</sup>

# 5.3.3. Computation of the power transfer function

Below we follow the description of the PTF technique given in. 50,51

The spectrum  $\phi(k,t)$  in Eq. (5.29) can be represented by its amplitude and phase. The amplitude is slowly varying in time compared with the phase changes  $\phi(k,t) = |\phi(k,t)|e^{i\Theta(k,t)}$ .

The spectrum change in time  $\frac{\partial \phi(k,t)}{\partial t}$ , can then be estimated using a differential approach:

$$\frac{\partial \phi(k,t)}{\partial t} = \lim_{\tau \to 0} \left( \frac{||\phi(k,t+\tau)| - |\phi(k,t)||}{\tau} \frac{1}{|\phi(k,t)|} + i \frac{\Theta(k,t+\tau) - \Theta(k,t)}{\tau} \right) \phi(k,t). \tag{5.36}$$

Substituting Eq. (5.36) into Eq. (5.29) and solving for  $\phi(k, t+\tau)$  (where  $\tau$  is very small), we obtain:

$$\phi(k, t + \tau) = \frac{\Lambda_k^L \tau + 1 - i[\Theta(k, t + \tau) - \Theta(k, t)]}{e^{-i[\Theta(k, t + \tau) - \Theta(k, t)]}} \phi(k, t) + \frac{1}{2} \sum_{\substack{k_1, k_2, \\ k = k_1 + k_2}} \frac{\Lambda_k^Q(k_1, k_2) \tau}{e^{-i[\Theta(k, t + \tau) - \Theta(k, t)]}} \times \phi(k_1, t) \phi(k_2, t),$$
(5.37)

where  $\Lambda_k^L = \gamma_k + i\varpi_k$ .

The spectrum at time  $t + \tau$ ,  $\phi(k, t + \tau)$  is thus defined by the spectrum  $\phi(k, t)$  at t through linear coefficient  $\Lambda_k^L$  and quadratic coefficient  $\Lambda_k^Q(k_1, k_2)$ . To simplify, the following definitions are used:

$$X_{k} = \phi(k, t), Y_{k} = \phi(k, t + \tau),$$

$$L_{k} = \frac{\Lambda_{k}^{L} \tau + 1 - i[\Theta(k, t + \tau) - \Theta(k, t)]}{e^{-i[\Theta(k, t + \tau) - \Theta(k, t)]}},$$

$$Q_{k}^{k_{1}, k_{2}} = \frac{\Lambda_{k}^{Q}(k_{1}, k_{2})\tau}{e^{-i[\Theta(k, t + \tau) - \Theta(k, t)]}},$$
(5.38)

where  $k = k_1 + k_2$ . Equation (5.37) can now be written as:

$$Y_k = L_k X_k + \frac{1}{2} \sum_{\substack{k_1, k_2, \\ k = k_1 + k_2}} Q_k^{k_1, k_2} X_{k_1} X_{k_2}$$
 (5.39)

The wave coupling equation Eq. (5.29) is thus related to a nonlinear system (described by Eq. (5.39)) in which the output  $Y_k$  is composed of linear and quadratic nonlinear responses to the input signal  $X_k$ .

Equation (5.39) is the simplest form of an equation which can be related to wave-wave coupling, assuming that the four-wave coupling and the higher order processes are much weaker than the three-wave coupling. The technique to derive coefficients  $L_k$  and  $Q_k^{k_1,k_2}$  of Eq. (5.39) from the measured fluctuation series will be described in the next subsection. These coefficients serve as fundamental quantities for the estimation of the growth rate, the wave-wave coupling coefficients, and eventually of the energy transfer in the spectrum.

The phase shift at wave number k between t and  $t+\tau$  can be estimated from the cross-power spectrum,

$$e^{-i[\Theta(k,t+\tau)-\Theta(k,t)]} = \frac{\langle Y_k X_k^* \rangle}{|\langle Y_k X_k^* \rangle|} . \tag{5.40}$$

The coupling coefficient  $\Lambda_k^Q(k_1, k_2)$  in Eq. (5.29) can be derived from the wave coupling coefficients  $L_k$  and  $Q_k^{k_1, k_2}$  as,

$$\Lambda_k^Q(k_1, k_2) = Q_k^{k_1, k_2} \frac{\langle Y_k X_k^* \rangle}{|\langle Y_k X_k^* \rangle|} \frac{1}{\tau} , \qquad k = k_1 + k_2 .$$
 (5.41)

256

Multiplying the wave coupling equation (5.29) by  $\phi^*(k,t)$ , we can write a wave kinetic equation for the spectral power  $P_k = \langle \phi_k \phi_k^* \rangle$  in terms of coupling coefficients  $\Lambda_k^L$  and  $\Lambda_k^Q(k_1, k_2)$ .

coupling coefficients  $\Lambda_k^L$  and  $\Lambda_k^Q(k_1, k_2)$ . Since  $\frac{\partial}{\partial t} [\phi(k, t) \phi^*(k, t)] = \frac{\partial \phi(k, t)}{\partial t} \phi^*(k, t) + \frac{\partial \phi^*(k, t)}{\partial t} \phi(k, t)$ , the wave kinetic equation can be written as:

$$\frac{\partial P_k}{\partial t} \approx 2\gamma_k P_k + \sum_{\substack{k_1, k_2, \\ k = k_1 + k_2}} T_k(k_1, k_2)$$
 (5.42)

The power transfer function  $T_k(k_1, k_2)$  quantifies the spectral power exchanged between different waves in the spectrum due to the three-wave coupling. It is related to the quadratic coupling coefficient, as

$$T_k(k_1, k_2) = Re \left[ \Lambda_k^Q(k_1, k_2) \langle \phi_k^* \phi_{k_1} \phi_{k_2} \rangle \right].$$
 (5.43)

The energy stored in the electrostatic fluctuations  $\phi_k$  can be expressed as  $W_k = (1 + k_\perp^2) |\phi_k|^2$ . The nonlinear energy transfer function can be defined as:

$$W_{NL}^{k} = (1 + k_{\perp}^{2}) \sum_{\substack{k_{1}, k_{2}, \\ k = k_{1} + k_{2}}} T_{k}(k_{1}, k_{2}), \tag{5.44}$$

The nonlinear energy transfer function (NETF),  $W_{NL}^k$  in Eq. (5.44), and the linear growth rate,  $\gamma_k$  in Eq. (5.42), are the main spectral quantities used in the experimental analysis of the spectral transfer.

# 5.3.3.1. Derivation of coupling coefficients (Ritz method)

The method of computing the coupling coefficients which characterize a nonlinear system described by a single input and a single output, has been proposed by Ritz et al.<sup>50</sup> The output of such a black-box system,  $Y_p$ , (in either spatial or in temporal domain) contains linear and quadratic responses to the input signal,  $X_p$ , in the form:

$$Y_p = L_p X_p + \sum_{\substack{p_1 > p_2 \\ p = p_1 + p_2}} Q_p^{p_1, p_2} X_{p_1} X_{p_2} + \epsilon_p$$
 (5.45)

where  $\epsilon_p$  is added to represent the noise in the signal.

Coefficients  $L_p$  and  $Q_p(p_1, p_2)$  quantify linear and quadratic responses. The subscript p in Equation (5.45) represents either the wave number k, or the frequency f, depending on a system.

We assume that the measured signals are stationary and that they can be divided into many statistically similar segments, the realizations. To derive the coupling coefficients, Eq. (5.45) is multiplied by the complex conjugate of  $X_p$ . Then by ensemble averaging over many realizations, denoted as <>, one obtains:

$$\langle Y_p X_p^* \rangle = L_p \langle X_p X_p^* \rangle + \sum_{\substack{p_1 > p_2, \\ p = p_1 + p_2}} Q_p^{p_1, p_2} \langle X_p^* X_{p_1} X_{p_2} \rangle.$$
 (5.46)

Here  $\langle Y_p X_p^* \rangle$  is the cross-power spectrum of the fluctuations,  $\langle X_p X_p^* \rangle$  is the auto-power spectrum.  $\langle X_p^* X_{p_1} X_{p_2} \rangle$  is the auto-bispectrum. Note that in Eq. (5.46), the cross-power spectrum term  $\langle \epsilon_p X_p^* \rangle$  is ignored since the cross-power spectrum (and any higher order spectrum, such as  $\langle \epsilon_p X_{p_1}^* X_{p_2}^* \rangle$  which will be encountered in the derivation of Eq. (5.47)) averages to zero between the signals and noise.

By multiplying Eq. (5.45) with  $X_{p_1}^{'*}X_{p_2}^{'*}$  and by ensemble averaging, we obtain a second equation which contains linear and quadratic transfer functions,

$$\left\langle Y_{p}X_{p_{1}}^{'*}X_{p_{2}}^{'*}\right\rangle = L_{p}\left\langle X_{p}X_{p_{1}}^{'*}X_{p_{2}}^{'*}\right\rangle + \sum_{\substack{p_{1} > p_{2}, \\ p = p_{1} + p_{2}}} Q_{p}^{p_{1}, p_{2}}\left\langle X_{p_{1}}X_{p_{2}}X_{p_{1}}^{'*}X_{p_{2}}^{'*}\right\rangle,$$

$$(5.47)$$

where  $p = p_1 + p_2 = p_1' + p_2'$ . Here  $\langle Y_p^* X_{p_1} X_{p_2} \rangle$  is the cross-bispectrum and  $\langle X_{p_1} X_{p_2} X_{p_1}'^* X_{p_2}' \rangle$  is the fourth-order moment.

Eq. (5.47) can be simplified by approximating the fourth-order moments  $\langle X_{p_1}X_{p_2}X_{p_1}'^*X_{p_2}'^*\rangle$  by the square of the second-order moments  $\langle |X_{p_1}X_{p_2}|^2\rangle$  (by neglecting terms with  $(p_1',p_2') \neq (p_1,p_2)$ ).<sup>50</sup> This approximation is based on the random-phase assumption, similarly to the weak turbulence theory.

Under this approximation, Eq. (5.47) is reduced to:

$$\langle Y_p X_{p_1} X_{p_2} \rangle = L_p \langle X_p X_{p_1} X_{p_2} \rangle + Q_p^{p_1, p_2} \langle |X_{p_1} X_{p_2}|^2 \rangle$$
 (5.48)

The determination of the coupling coefficients  $L_p$  and  $Q_p^{p_1,p_2}$  is usually not straightforward: a set of dependent equations (5.46) and (5.48) need to be solved iteratively.

An example where the coupling coefficients can be easily determined is a Gaussian input signal. For a Gaussian signal, the auto-bispectrum goes to zero,  $\langle X_p X_{p_1} X_{p_2} \rangle = 0$  such that the coupling coefficients  $Q_p^{p_1,p_2}$  and  $L_p$  are simply determined from Eq. (5.48).

However, many systems such as turbulent fluids and plasmas, do not allow such a restrictive assumption about the input signal. Generally, the input should not be considered Gaussian because of the nonlinear history of the fluctuations.

### 5.3.3.2. Derivation of coupling coefficients: modified Ritz method

Applications of the technique described above sometimes yield unphysically large transfer coefficients for the measured fluctuation data. This problem may arise because the method does not account for the non-ideal fluctuations. For example, Eq. (5.45) contains only linear response and the three-wave interactions. Turbulence may contain spectral components which do not participate in the wave coupling described by Eq. (5.45). The higher-order nonlinear coupling (e.g., fourth-order, or higher), systematic errors, etc., may also need to be taken into consideration. To address this problem, a modified method has been proposed.  $^{53}$ 

In the modified method, the measured spectra  $(X_p, Y_p)$  are represented as the sum of an ideal spectrum  $(\beta_p, \alpha_p)$ , which is driven by linear and quadratic processes, and a non-ideal spectrum  $(X_p^{ni}, Y_p^{ni})$  whose components are not involved in the linear and the three-wave coupling processes:

$$X_p = \beta_p + X_p^{ni}, \quad Y_p = \alpha_p + Y_p^{ni}.$$
 (5.49)

The non-ideal spectrum  $(X_p^{ni}, Y_p^{ni})$  is assumed to be completely uncorrelated with the ideal fluctuation spectrum  $(\beta_p, \alpha_p)$ , which is reasonable for the noise or any spectrum not described by Eq. (5.45).

Using Eq. (5.49), equation (5.39) can be rewritten in the form

$$Y_p - Y_p^{ni} = L_p(X_p - X_p^{ni}) + \sum_{\substack{p_1 \ge p_2, \\ p = p_1 + p_2}} Q_p^{p_1, p_2}(X_{p_1} - X_{p_1}^{ni}) \times (X_{p_2} - X_{p_2}^{ni}).$$

$$(5.50)$$

The same procedure as in the original method is applied to Eq. (5.50). First, Eq. (5.50) is multiplied by  $X_p^*$  and  $X_{p'_1}^*X_{p'_2}^*$  respectively. Then, the ensemble averaging over many statistically similar realizations is performed. In the two equations obtained, the terms with cross terms containing the non-ideal spectrum can be removed due to the zero-correlation assumption. The exceptions are the auto-power spectra  $\langle \beta_p \beta_p^* \rangle$ ,  $\langle \alpha_p \alpha_p^* \rangle$ . As a result, the following set of equations is obtained, <sup>53</sup>

$$\langle Y_{p}X_{p}^{*}\rangle = L_{p}\langle \beta_{p}\beta_{p}^{*}\rangle + \sum_{\substack{p_{1} \geq p_{2}, \\ p = p_{1} + p_{2}}} Q_{p}^{p_{1}, p_{2}}\langle p_{p_{1}}X_{p_{2}}X_{p}^{*}\rangle,$$

$$\langle \alpha_{p}\alpha_{p}^{*}\rangle = L_{p}\langle X_{p}Y_{p}^{*}\rangle + \sum_{\substack{p_{1} \geq p_{2}, \\ p = p_{1} + p_{2}}} Q_{p}^{p_{1}, p_{2}}\langle X_{p_{1}}X_{p_{2}}Y_{p}^{*}\rangle,$$

$$\langle Y_{p}X_{p_{1}}^{*}X_{p_{2}}^{*}\rangle = L_{p}\langle X_{p}X_{p_{1}}^{*}X_{p_{2}}^{*}\rangle$$

$$+ \sum_{\substack{p_{1} \geq p_{2}, \\ p = p_{1} + p_{2} = p_{1}^{'} + p_{2}^{'}}} Q_{k}^{p_{1}^{'}, p_{2}^{'}}\langle X_{p_{1}^{'}}X_{p_{2}^{'}}X_{p_{1}}^{*}X_{p_{2}}^{*}\rangle,$$

$$(5.51)$$

An additional relationship is required to complete the set of equations needed for the derivation of the four unknown variables,  $L_p, Q_p^{p_1, p_2}, \langle \beta_p \beta_p^* \rangle, \langle \alpha_p \alpha_p^* \rangle$ . The power spectrum is considered stationary for fully developed turbulence:

$$\langle \beta_p \beta_p^* \rangle = \langle \alpha_p \alpha_p^* \rangle \tag{5.52}$$

The fourth-order moment  $\langle X_{p_1'} X_{p_2'} X_{p_1^*} X_{p_2^*} \rangle$  is either retained, or it is substituted using the approximation  $\langle X_{p_1} X_{p_2} X_{p_1}'^* X_{p_2}'^* \rangle = \langle |X_{p_1} X_{p_2}|^2 \rangle$  as discussed above.

# 5.3.4. Amplitude correlation technique

The amplitude correlation is a spectral transfer analysis technique which in many aspects complements the PTF method. The amplitude correlation was first applied to the measurement of nonlinear interactions between drift waves and low-frequency flute-like modes.<sup>55</sup> The nonlinear interactions in which two drift waves interact with the low-frequency flute-like mode were identified as the mechanism responsible for the drift-wave saturation. Later, the method was applied to study the 'frequency doubling' interaction drift waves. The justification of the method was given in reference.<sup>56</sup>

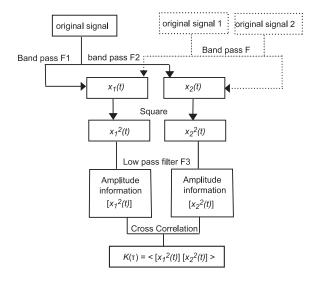


Fig. 5.10. The flow chart of the amplitude correlation technique

The basic idea of the amplitude correlation is to obtain a new signal from a fluctuation signal. This new signal represents the time-envelope of the original signal in a particular frequency band. This envelope signal can then be cross-correlated with other envelope signals derived in a similar way. The resulting maximum correlation between the two signals and the time delay of the maximum correlation are indicative of the degree of coherent coupling and of the energy flow direction between the two frequency bands.

The procedure is illustrated schematically in Fig. 5.10. From the original fluctuation signal x(t), two time series,  $x_1(t)$  and  $x_2(t)$ , are obtained by applying two band-pass filters  $F_1$  and  $F_2$  centered on frequencies  $f_1$  and  $f_2$  respectively to the signal. These two time series,  $x_1(t)$  and  $x_2(t)$ , are then squared and passed through a low-pass filter  $F_3$  to obtain the slow varying amplitude components denoted as  $[x_i^2(t)], i = 1, 2$ . Then the cross-correlation function (CCF) between these signals is computed as

$$K(\tau) = \left\langle \left[ x_1^2(t) \right] \left[ x_2^2(t+\tau) \right] \right\rangle \tag{5.53}$$

where the angle brackets <> denote ensemble average.

If the original signals  $x_1$  and  $x_2$  contain frequencies  $\omega_{1,2} \pm \Delta \omega$ , the squared signals would contain high-frequency bands centered around  $2\omega_{1,2}$  and a low-frequency band extending from zero to  $2\Delta\omega$ . It is this low-frequency band that contains the amplitude information and the purpose of the filter  $F_3$  is to remove the upper band. It also serves to remove the mean values of  $x_{1,2}^2$ .

 $K(\tau)$  can be used for intuitive interpretations. For example, in a wave propagation experiment using the amplitude correlation, applying identical filters  $F_1$  and  $F_2$  to signals from probes separated in space, a direct measurement of the group velocity of waves in the selected frequency band can be obtained.<sup>56</sup> One of the most important usages of the amplitude correlation method is determination of the energy flow in a turbulent spectrum.

The direction of the energy flow from one frequency domain to the other can be determined from the sign of the time delay  $(\tau_{lag})$  of the peak value of the cross-correlation function  $K(\tau)$ . The two domains are defined by the two bandpass filter  $F_1$  and  $F_2$ . Positive time lag means the first signal  $x_1(t)$  leads the second signal  $x_2(t)$  in phase. As a result, one can speculate that the frequency domain around  $F_1(x_1(t))$  could be the energy source of that of  $F_2(x_2(t))$ . Similarly, a negative time lag  $\tau$  suggests that the region around  $x_2(t)$  is the energy supplier for  $x_1(t)$ . The amplitude correlation method can, in principle, help to estimate the growth/damping rate of the driven mode and the nonlinear energy throughput rate.

In the applications of the amplitude correlation technique, the two frequency bands under consideration do not necessarily need to come from the same fluctuation signal. Nonlinear interaction between different fluctuation fields can also be detected through this method.

An important issue in interpreting the time lag is that the time delay,

 $\tau_{lag}$ , is indicative of the energy flow between the two frequency bands only when the two frequency bands are strongly correlated.

# 5.4. Experimental evidence of the inverse energy cascade in plasma

In this section we illustrate how the above methods of the spectral transfer analysis are applied to experimental data. The examples are based on the results from the H-1 toroidal heliac. $^{57,58}$ 

## 5.4.1. Applicability of the nonlinear spectral transfer model

The wave coupling equation, Eq. (5.29), describes turbulence in which a single-field description is valid and the three-wave interactions are permitted and dominant. A distinct feature of plasma as a continuous medium is that the responses of the electrons and ions are not identical, hence they induce collective electromagnetic fields. The dynamical equations for a plasma in the fluid limit are usually constructed using a two-fluid picture.

A single-field description of the plasma turbulence needs to be justified on a case-to-case basis. Consider the electrostatic wave turbulence, when the magnetic field fluctuations can be neglected. In a stable drift wave, electrons relax, along the magnetic field, to acquire Boltzmann distribution in the wave potential:

$$\tilde{n}_e = n_0 \exp(e\tilde{\phi}/T). \tag{5.54}$$

When the drift wave becomes unstable, the electron response is perturbed. This perturbation is characterized by the so-called non-adiabatic electron response,  $\delta n_e$ . If the normalized level of the potential fluctuations is small,  $(e\bar{\phi}/T) << 1$ , this can be written as

$$\tilde{n}_e = n_0 (e\tilde{\phi}/T) + \delta n_e. \tag{5.55}$$

In the unstable wave  $\delta n_e \neq 0$  and the  $n_e$  and  $\phi$  fluctuations are out of phase. This phase shift can be detected in experiment.

For a single-field description to be valid, the  $n_e$  and  $\phi$  fluctuations should be in phase. A well-known example is the Hasegawa-Mima model (see Section 1.4 of Chapter 4) where  $\delta n_e = 0$ . This also means that the fluctuation-driven particle flux is zero. As follows from Equation (5.11),

$$\Gamma_{fl} = \frac{2}{B} \int_{0}^{\infty} d\omega \left[ P_{nn} P_{EE} \right]^{1/2} |\gamma_{nE}| \cos \left[ \alpha_{nE} \right] = 0,$$

since  $\tilde{n}_e$  and  $\tilde{E}_{\theta}$  have a  $\pi/2$  phase shift  $(\tilde{E}_{\theta} = -\nabla_{\theta}\tilde{\phi})$  and  $\cos(\alpha_{nE}) = 0$ .

While confirming the phase difference between  $\tilde{n}_e$  and  $\tilde{\phi}$ , it should be kept in mind, that it is fluctuations in the *plasma* potential, rather than in the *floating* potential which should be analyzed. In other words, fluctuations in the electron temperature should be included (see Eq. (5.7)).

Fig. 5.11. (c) shows the phase shift between fluctuations  $\phi_p$  and  $\phi_f$  obtained from the experimental data in H-1. The phase shift between the two fluctuating quantities is close to zero in the broad spectral range from  $f \approx 0$  to 60 kHz. For the spectral energy transfer analysis, the phase information is much more important than the amplitude, since most of the spectral quantities used in the analysis (e.g. auto- and cross-bicoherence) are normalized.

In the given example from the H-1 heliac,  $\tilde{\phi}_f$  and  $\tilde{\phi}_p$  are in phase and the analysis can be simplified:  $\tilde{\phi}_f$  is used in the PTF analysis.

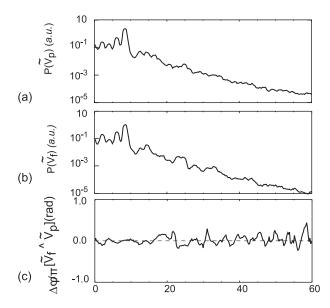


Fig. 5.11. Power spectra of (a) fluctuations in the plasma potential  $\tilde{\phi}_p$ , and (b) fluctuations in the plasma floating potential  $\tilde{\phi}_f$ . (c) Spectra of the phase shift between  $\tilde{\phi}_p$ , and  $\tilde{\phi}_f$ .

The phase difference between fluctuations in the poloidal electric field,  $\tilde{E}_{\theta}$ , and the density,  $\tilde{n}_{e}$  is shown in Fig. 5.12.. This phase shift is close to  $\pi/2$  over the most of the spectrum suggesting that the electron response is adiabatic. Thus, the applicability of the single-field description in the described experiments is justified.

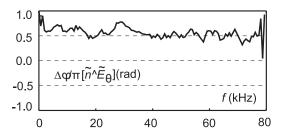


Fig. 5.12. Spectrum of the phase shift between fluctuations in the electron density,  $\tilde{n}_e$ , and poloidal electric field,  $\tilde{E}_{\theta}$ .

Another point which should be made here is that in experiments, spectra are measured in the frequency (f) domain, while the wave kinetic equation is defined in the wave number (k) domain. The PTF analysis of experimental data would only be valid if a linear k-f relationship is confirmed experimentally. Below we illustrate how this can be done in experiment.

In the laboratory frame of reference, frequencies of the fluctuations are Doppler shifted due to the presence of the  $E \times B$  drift in practically all toroidal plasmas:  $\omega_{lab} = \omega_{plasma} + k_{\theta}V_{E\times B}$ . As explained in Section 2.5, in most cases,  $E \times B$  drift dominates over the phase velocity in the plasma frame. Thus, the fluctuation frequencies in the lab frame are proportional to the poloidal wave numbers of the fluctuations. Since in the broadband turbulence the wave number spectra are isotropic,  $k_{\theta} \approx k_r$ ,, one can assume that  $k \approx \sqrt{2}k_{\theta} \propto \omega$ . The  $E \times B$  Doppler shift plays in such cases a role of the wave number spectrograph.

## 5.4.2. Results on the spectral transfer analysis

Figure 5.13. shows the power spectrum of the  $\phi_f$  fluctuations in the H-1 plasma.<sup>57</sup> Spectral power decreases with frequency in the range f=(0-80) kHz. In the frequency range of f<20 kHz several coherent modes are observed.

Before applying the power transfer analysis technique to the fluctuation data, the linear k-f relationship needs to be tested, as discussed above.

Wave numbers of fluctuations are measured using two poloidally separated probes, as  $k_{\theta} = \Delta \phi/\Delta y$ , where  $\phi$  is the phase shift and  $\Delta y$  is the distance between the probes. This wave number  $k_{\theta}$  is shown as a function of frequency,  $k_{\theta}(f)$ , in Fig. 5.13. (b). Though the  $k_{\theta}(f)$  plot has large ripple, a linear trend, represented using a black line, is clearly observed.

The fluctuation phase velocity in the poloidal direction,  $V = \omega_{lab}/k_{\theta}$ , derived from this linear fit agrees within 10% with the measured  $\mathbf{E} \times \mathbf{B}$ 

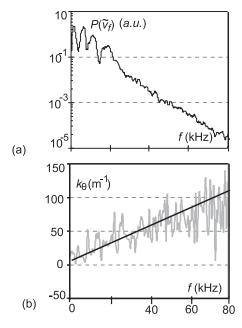


Fig. 5.13. (a): Power spectrum of the fluctuations in the floating potentials,  $\tilde{V}_f$ , (b) measured poloidal wave number spectrum  $k_{\theta}(f)$  (grey line) with the linear fit (black line)

drift velocity in this radial region, confirming that  $k_{\theta}V_{E\times B} >> \omega_{plasma}$ .

Thus, the spectral power transfer can be studied in the frequency domain. The three-wave interactions satisfying matching rules for the wave numbers,  $k = k_1 + k_2$ , also obey the frequency selection rule,  $f = f_1 + f_2$ .

It should be noted, that while estimating the temporal evolution of the turbulence spectra, one needs to take into account that turbulence drifts in the lab frame. As discussed in Section 3.3, the change in the turbulence spectrum is estimated using the differential approach represented by Eq. (5.36). During the time interval,  $\tau$ , turbulence will drift in poloidal direction by  $\Delta y = \tau V_{\mathbf{E} \times \mathbf{B}}$ . As a result, the turbulence evolution should be studied using two probes separated poloidally. The time delay,  $\tau$ , in the Equation (5.36) should be estimated using the distance between the probes,  $\Delta y$ , and  $V_{\mathbf{E} \times \mathbf{B}}$ .

The nonlinear energy transfer function (NETF),  $W_{NL}^k$ , and the linear growth rate,  $\gamma_k$ , derived from Eq. (5.42) in Section 5.3.3. are shown in Fig. 5.14..  $W_{NL}^k$  is negative in the broadband spectral region of  $f = (20 - 1)^{-1}$ 

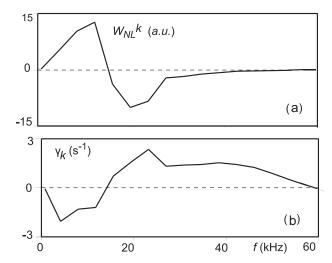


Fig. 5.14. (a) The nonlinear energy transfer function  $W_{NL}^k$ ; (b) linear growth rate  $\gamma_k$  derived from Eq. (5.42). The frequency resolution is  $\Delta f \approx 4$  kHz.

50) kHz suggesting that waves in this range on-average lose energy, whereas the lower frequency spectral range (f < 20 kHz) gains spectral energy due to the three-wave interactions. The linear growth rate shown in Fig. 5.14. (c) has positive maximum at  $f \approx 25$  kHz. This spectral range is the range where initially unstable waves develop.

The NETF shown in Fig. 5.14. illustrates the *inverse energy cascade* in the broadband turbulence. Its computation required substantial statistical averaging. The turbulence signals digitized at the rate of 1 MHz during 80 ms of the plasma discharge are divided into 460 overlapping segments, such that the spectral moments needed for the PTF computation are then averaged over these segments. Such averaging is needed to correctly estimate spectral transfer via the random-phase wave interactions.<sup>58</sup>

The inverse energy cascade is the mechanism of spreading spectral energy from the instability range into a broad range of the wave numbers and frequencies. The PTF method<sup>50,53</sup> has been successfully used to demonstrate the existence of the inverse energy cascade in toroidal plasma.<sup>57,58</sup> However, the NETF in Fig. 5.14.(a) does not show the fine structure, which would correspond to coherent spectral features seen in the spectrum of Fig. 5.13.(b). This may be suggestive of the non-cascade origin of these features.

# 5.5. Quasi-two-dimensional turbulence in fluids and plasma and generation of zonal flows

The inverse energy cascade in 2D fluid turbulence<sup>42</sup> is the flow of spectral energy from smaller to larger scales, leading to the  $E_k \propto k^{-5/3}$  scaling of the energy spectrum in this spectral range (see Chapter 1, Section 4, by G. Falkovich). R. Kraichnan has predicted that the spectral energy may pile up at the largest scale allowed by the system size and noted a similarity between the condensation of the turbulent energy and the Bose-Einstein condensation of the 2D quantum gas.<sup>42</sup> The condensate formation in 2D fluids has been confirmed in experiments<sup>59,60</sup> and in numerical simulations,<sup>61,62</sup> for review see.<sup>63</sup> Below we illustrate how turbulence condenses in the 2D fluid experiment.

In plasma, quasi-2D turbulence can also be generated via 3-wave interactions.<sup>8</sup> The structure of the Hasegawa-Mima equation, which describes spectral evolution of the drift-wave turbulence, is identical to the Charney equation describing the evolution of nonlinear Rossby waves in planetary atmosphere.<sup>9,64</sup> These models, similarly to the models of the 2D fluid turbulence described by the 2D Navier-Stokes equation, have two conserved quantities, energy and enstrophy. As a consequence, there are two inertial ranges which correspond to (a) the inverse cascade of energy, and (b) forward cascade of enstropy. Similarly to the fluid dynamics in 2D, spectral energy in plasma can condense in the largest scale.<sup>9,65</sup> In particular, such condensation may lead to the formation of zonal flows and other coherent structures which is a form of the plasma self-organization.<sup>66</sup> We will illustrate generation of zonal flow in plasma experiment and will discuss experimental signatures of such flow.

### 5.5.1. Spectral condensation of 2D turbulence

One of the first convincing experimental evidence of the inverse energy cascade in 2D turbulence was presented by J. Sommeria in 1987.<sup>59</sup> In this experiment, turbulence was generated in a thin layer of mercury in a cell. The fluid was placed in the vertical magnetic field. 36 biased electrodes of varying polarity generated electric currents in a layer which, by interacting with the vertical magnetic field generated 36 planar vortices in a cell. By varying the current and the depth of the mercury layer, the forcing and the linear damping could be finely controlled. Sommeria observed the  $k^{-5/3}$  scaling due to the inverse cascade in the energy inertial range (though in a rather narrow k-range) and also reported the observation of the largest vortex limited by the cell size at low linear dissipation due to the process of the spectral condensation.

Detailed measurements of the spectral energy scaling were presented by Paret and Tabeling<sup>60,67</sup> in 1997-98 in experiments in the stratified layers of electrolyte. In these experiments 2D turbulent flows were studied by generating  $J \times B$ -driven vortices in thin layers of fluid. These experiments have confirmed the existence of the inverse energy cascade in the quasi-2D turbulence, the  $k^{-5/3}$  scaling, as predicted by Kraichnan,<sup>42</sup> and also have confirmed the generation of the spectral condensate at low damping.

The most recent experiment in which the spectral condensation of turbulence was reproduced, has been aimed at the comparison between fluid and plasma turbulence.<sup>68</sup> Below we summarize some of these results.

Figure 5.15. shows experimental setup used in references<sup>60</sup> and reproduced in.<sup>68</sup> Turbulence is generated via the interaction between  $J \times B$ -driven vortices whose sizes and the distances between their centres (positions of the magnetic dipoles) determine the scale at which energy is injected into the system. This scale is characterized by the wave number  $k_i$ . The flow on the free surface of the light fluid is visualized by placing small latex particles on the surface and by recording their trajectories using video camera. The particle image velocimetry (see Chapter 7 by J. Soria) allows the velocity and the vorticity fields to be reconstructed from the consecutive images of the particles in the flow.

After the current is turned on, and if the vortex interaction energy is sufficiently high, the inverse energy cascade leads to the aggregation of the spectral energy at larger and larger scales. The maximum of the energy spectrum thus moves from  $k_i$  toward the lower-k range of the wave numbers. In the absence of the energy dissipation, a wave number corresponding to the maximum spectral energy,  $k_m$ , can not be constant in time. However, if there is damping for large scales, for example via linear damping  $\mu$ ,  $k_m$  stabilizes at

$$k_m \approx \left(\frac{\mu^3}{\epsilon}\right)^{1/2},$$
 (5.56)

where  $\epsilon$  is the energy dissipation rate (see Chapter 1).

Another characteristic scale in 2D turbulence is determined by the size of the system,  $k_s$ , such as the size of the fluid cell. If the system size is larger than the resistive scale, or,  $k_s < k_m$ , one should observe the stationary spectrum which has a maximum at  $k_m$ . If however the resistive wave number [Eq. (5.56)] is larger than the cell size,  $k_s > k_m$ , spectral condensation of turbulence becomes possible when spectral energy accumulates at the system size. This is illustrated schematically in Fig. 5.16..

The evolution of the turbulent 2D flow in a cell is shown in Fig. 5.17. for the case when the damping to the bottom of the fluid cell is reduced due to the fluid stratification, such that the spectral condensation of turbulence 268

#### Michael Shats and Hua Xia

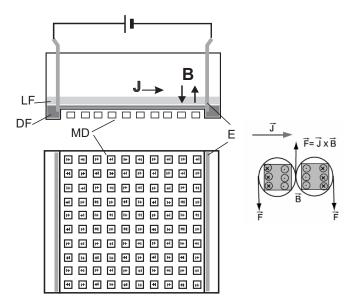


Fig. 5.15. Schematic of the electromagnetically-driven 2D turbulence in electrolyte. A thin layer of a light fluid (LF) rests on the layer of denser fluid (DF). A matrix of  $10\times 10$  magnetic dipoles (MD) is placed under the bottom of the fluid cell. Current J flowing between two electrodes (E) generates 100 vortices due to the  $J\times B$  force, as illustrated on the right.

is possible. Initially only externally forced vortices are seen [Fig. 5.17.(a)]. The inverse energy cascade destroys these vortices and leads to the generation of a broadband spectrum of eddies seen in Fig. 5.17.(b). At some stage, a large vortex is formed, which then persists in steady-state as shown in Fig. 5.17.(c).

The corresponding evolution of the wave number spectra, derived from the velocity field of the trace particles, is illustrated in Fig. 5.18.. At the early stage of the flow evolution,  $t=t_1$ , spectrum shows a peak at the forcing scale,  $k=k_i$ . Later, at  $t=t_2$ , this peak is washed out and the maximum of the spectral energy shifts to lower k. Eventually spectral energy is accumulated at  $k_s$  which represents the scale of the large vortex shown in Fig. 5.17.(c).

It should be noted, that the increase in spectral energy in the condensate wave number range at  $t = t_3$  coincides with the reduction in spectral energy in the broadband turbulence, including the forcing range  $k_i$ .

After the formation of the largest vortex, the condensate persists in steady-state. The energy necessary to overcome damping at this largest scale can only come from the energy source at  $k_i$ . The fact that spectral

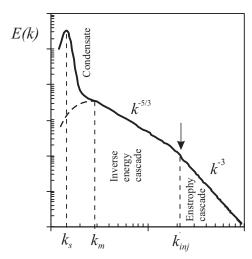


Fig. 5.16. Schematic of the 2D turbulence spectrum.

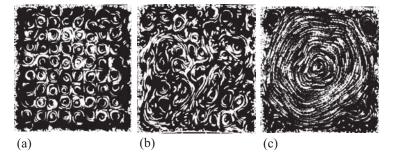


Fig. 5.17. Trajectories of the tracer particles averaged over 12 frames of recorded video during spectral condensation of turbulence. (a) The initial stage, t=3 seconds after switching on the current; (b) the inverse energy cascade stage, t=16 s; (c) steady-state spectral condensate stage, t=55 s.

energy in the spectral range  $k_s < k$  is reduced in the presence of the condensate may be indicative of the stronger spectral coupling between spectral regions of  $k_i$  and  $k_s$ , such that the spectral energy is delivered from  $k_i$  to  $k_s$  directly, rather than through a multi-step process of the energy cascade.

## 5.5.2. Zonal flows in plasma turbulence

In the above example we have seen that strong anisotropic flow may develop as a result of accumulation of the turbulent energy of the 2D turbulence

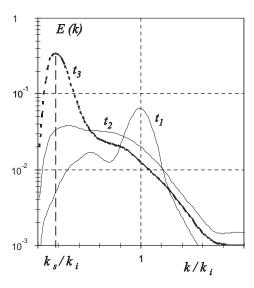


Fig. 5.18. Wave number spectra of the velocity field during the development of spectral condensate in 2D fluid.  $t_3 > t_2 > t_1$ .

at low wave numbers. Understanding physics of such an interplay between stationary flows and turbulent fields is also important in plasma turbulence studies (for review see<sup>69</sup>). In addition to flows driven by the momentum input (or loss), turbulence-driven flows play important roles in the plasma dynamics. A complex interplay between turbulence and flows in magnetically confined plasma has been a focus of the turbulence related studies in the last two decades. This topic is of great practical importance, due to its relevance to such phenomena as improvement of the plasma confinement and formation of the plasma barriers. We will only briefly discuss this topic in these lectures.

First, it is important to clarify which flow is the most important in this context, since in plasma, unlike in neutral fluids, a number of flows appear (electron and ion diamagnetic drifts,  $E \times B$  drift, etc.). Out of them, the  $E \times B$  flow has unique status in plasma physics and it also has a central role in the plasma-flow interaction physics.

It has been shown theoretically  $^{70}$  in the equations governing electrostatic turbulence, the only convective term in the equations is the  $E \times B$  drift. The  $E \times B$  flow is the sole advectant of fluctuations in density, temperature, and flow. As explained in,  $^{69}$  this statement is a result of empirical observations and careful theoretical calculations. It does not simply follow from the fact that the  $E \times B$  drift velocity is the same for all particles regardless of their charge or mass, simply because this is not universally

correct, for example in complex magnetic geometry. A good illustration of the difference in the  $E \times B$  flow and in the ion mass flow velocities is given in.<sup>71</sup> What is important for us here is the fact that it is the  $E \times B$  flow, rather than bulk plasma flow, which is relevant in the turbulence-flow interaction.

In toroidal plasma the  $E \times B$  flow is determined by the radial component of the electric field. Radial electric field in the plasma can be estimated using the radial force balance equation (related to the ion momentum balance). This equation can be expressed as<sup>69</sup>

$$E_r = \frac{1}{q_i n_i} \frac{\partial}{\partial r} p_i + \frac{m_i}{q_i} \frac{\partial}{\partial r} \langle \tilde{u}_{\theta i} \tilde{u}_{ri} \rangle - u_{\theta i} B_{\phi} + u_{\phi i} B_{\theta}, \qquad (5.57)$$

where  $q_i$  is the ion charge,  $n_i$  is the ion density,  $m_i$  is the ion mass and  $u_i$  is the ion velocity. Subscripts  $\theta$  and  $\phi$  indicate poloidal and toroidal components of the flow velocities and of the magnetic field. The second term on the right-hand-side is the Reynolds stress. Reynolds stress in the fluid turbulence is discussed by J. Jiménez in Chapter 6 (Section 3). Reynolds stress in the plasma<sup>26</sup> (for review see<sup>69</sup>) provides a mechanism of generating stationary flows by turbulence.

Some of these flows have already been mentioned. These are zonal flows, or poloidally and toroidally symmetric potential structures driven by the plasma fluctuations. Reynolds stress is not the only theoretical mechanism which can drive zonal flows (see Chapter 4, Lecture 3). Poloidal and toroidal symmetry means that the poloidal and toroidal components of the wave number are zero:  $k_{\theta} = k_{\phi} = 0$ , while their radial wave number,  $k_r$ , remains finite. Such a structure is shown schematically in Fig. 5.19.. Arrows indicate the direction of the flow in poloidal plasma cross-section. Once again, the flow here is the  $E \times B$  flow, which does not coincide with the ion flow whose velocity  $u_{\theta i}$  appears in the radial force balance, Equation (5.57).

Theories of zonal flows in plasma are discussed in Lecture 3 by J. Krommes (see Chapter 4). For detailed review on the theory of zonal flows see. <sup>10</sup> Experimental studies of zonal flows are described in references. <sup>11–17</sup> The most recent collection of experimental results on zonal flows has been published in the special issue of the Plasma Physics and Controlled Fusion journal (Volume 48, Number 4, April 2006).

It is impossible to overview experimental results on the zonal flows in toroidal plasma in this section, however, it seems appropriate to illustrate how zonal flows are identified in experiments. Sometimes, geodesic acoustic modes, or GAMs are also referred to as the higher frequency branch of zonal flows (see Section 3.5 of Chapter 4). These modes appear in toroidal plasma, and are observed as the finite-frequency coherent potential structures. They will not be discussed here.

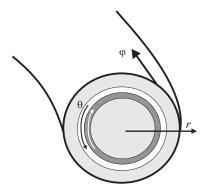


Fig. 5.19. Schematic of the zonal flow in toroidal plasma.

First we discuss experimental evidence of the stationary ( $f_{ZF} = 0$ ) zonal flows. There are two theoretically expected mechanisms of the zonal flow generation in plasma, which seem to be supported by observations. The first one is the generation of zonal flow via the inverse energy cascade in broadband turbulence of drift waves (see<sup>10</sup>). This mechanism is somewhat similar, but not identical, to the inverse energy cascade in 2D fluid turbulence described in the previous subsection. The second mechanism of the zonal flow generation is modulational instability whose theory is described in Section 3.1 of Chapter 4 by J. Krommes.

In the high-temperature plasma, the first observation of the stationary zonal flow whose frequency was very close to zero,  $f_{ZF} \approx 0$ , was reported in the CHS torsatron<sup>15</sup> by Fujisawa *et al.* Two heavy ion beam probe diagnostics (see Section 2.7) were set at two toroidal locations, such that the toroidal mode number n=0 of the observed  $f\approx 0$  potential structure could be confirmed experimentally.

Similar spectral feature has been also observed in the low-temperature plasma in the H-1 heliac using Langmuir probes.<sup>72</sup>

Spectrally broadened low-frequency band around  $f_{ZF}=0$  has signatures of zonal flow. Poloidal and toroidal mode numbers have been estimated from poloidally (1 and 2) and toroidally separated (2 and 3 probes). It is usually difficult to align toroidally separated probes to exactly the same poloidal position. As a result, a phase shift between probes 1 and 3 will occur due to the uncertainty in the poloidal separation between the probes,  $\Delta y_{13}$ :

$$\Delta\varphi_{13}(f) = k_{\parallel}(f)\Delta L_{\parallel} + k_{\theta}(f)\Delta y_{13}, \tag{5.58}$$

where  $\Delta L_{\parallel}$  and  $y_{13}$  are toroidal and poloidal separation between probes 1 and 3 respectively, and  $k_{\parallel}(f)$  is known from the phase difference between

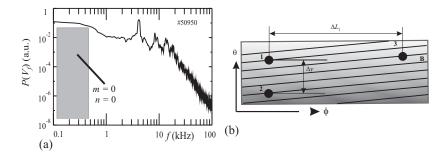


Fig. 5.20. (a) Frequency spectrum of electrostatic potential. Shaded f < 0.5 kHz frequency band corresponds to m = n = 0 zonal flow. (b) Probe setup used for identification of poloidal and toroidal mode numbers.

probes 1 and 2. In case of zonal flow, m=0, and the second term on the right-hand side becomes zero (since  $k_{\theta}=0$ ), such that the poloidal uncertainty  $\Delta y_{13}$  becomes unimportant and the toroidal wave number can be reliably estimated by measuring  $\Delta \varphi_{13}$ .

Accumulation of spectral energy in the spectrally broadened zero-frequency zonal flow illustrated in Fig. 5.20.(a) possibly occurs via the inverse energy cascade (see Section 4.2). It has been suggested in reference,  $^{68}$  that the processes of spectral condensation in 2D fluid turbulence (section 5.1) may be in several aspects similar to the generation of zonal flows in turbulent plasma. Experimental data  $^{68}$  generally agree with the theoretically proposed idea that the spectral energy is gradually accumulated in larger scales by cascading from the unstable spectral range (injection scale in 2D fluid), until the largest structure, or zonal flow develops. At this stage, the spectral transfer may be changing from spectrally local (wave numbers participating in the energy cascade are comparable) to non-local, such that the energy can be delivered into zonal flow directly from the unstable range scales  $k_{ur} >> k_{ZF}$ . Such a possibility has been proposed in  $^{73}$  and has been reviewed in.  $^{66}$ 

Generation of zonal flow via the modulational instability (Chapter 4, Section 3.1) is another possible scenario. The first experimental evidence of the zonal flow development which is consistent with this has been reported in.<sup>74</sup> In this case, zonal flow develops in the improved confinement mode (H-mode), in which the level of the broadband turbulence was substantially reduced. The generation of zonal flow was correlated with the development of the secondary instability in the plasma. This instability is driven by the  $E_r$  shear and is similar to the Kelvin-Helmholtz instability. Initially coherent oscillations appear at f=15 kHz. As the instability develops and the fluctuation spectrum becomes broader, a low frequency  $E_r$  spectral feature

develops, as illustrated in Fig. 5.21.. Zonal flow is the spectral feature at  $f \approx 1$  kHz seen in the wavelet plot of the  $E_r$  fluctuations of Fig. 5.21.(a). Corresponding 1 kHz feature in the fluctuations of  $E_{pol}$  (Fig. 5.21.(b)) is considerably weaker, since for zonal flows  $k_r >> k_\theta \approx 0$ . In this example,

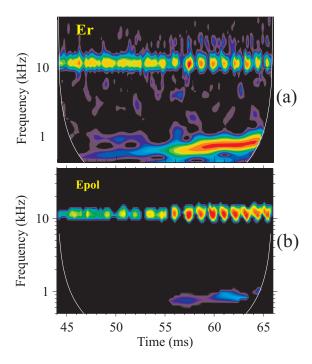


Fig. 5.21. Wavelet plots of the time evolution of the fluctuations in (a) radial and (b) poloidal electric fields. For details see.  $^{74}$ 

zonal flow has low but finite frequency, as is expected from the theory of the modulational instability (see paper by R. L. Dewar and R. F. Abdullatif, in the *Workshop Proceedings*).

## 5.6. Conclusion

In this chapter we gave a brief introduction to modern methods and results in experimental studies of turbulence in the plasma confined by toroidal magnetic field. Considerable progress has been made due to novel sophisticated diagnostics and analysis techniques, but also due to closer interaction between plasma theory, numerical simulations and experiments. This is particularly true with regard to studies of large turbulence-driven struc-

tures in plasma, such as zonal flows, geodesic acoustic modes, streamers etc. We have not even attempted to review all experimental results related to these topics in two lectures.

Several fundamental questions however remain unresolved. Among them is the role of turbulent fluxes in the net particle and energy transport. Answers to this question remain controversial. Though it is common to believe that turbulence generates fluxes which can affect net fluxes, it is clear that in some situations the role of turbulence is limited to the generation of strongly sheared  $E \times B$  flows in the plasma. In this case the improvement in particle confinement may be achieved due to, for example particle orbit squeezing. To some extent this agrees with recent theoretical ideas about intimate interrelation between neoclassical and turbulent fluxes in plasma.  $^{75}$ 

Understanding plasma turbulence can be greatly enhanced through interdisciplinary comparative studies of plasma and fluid turbulence. In this chapter we have illustrated one of the first attempts in this direction, which we find appropriate for this cross-disciplinary collection of lectures on turbulence.

The authors thank G. Conway for his valuable comments.

## **Bibliography**

- D. Bohm. In A. Guthrie and R. K. Wakerling, editors, The Characteristics of Electrical Discharges in Magnetic Fields, volume 1 of National Nuclear Energy Series, page 77. McGraw-Hill Book Company, Inc., New York, 1949.
- A. B. Mikhailovskii. Instabilities in a confined plasma. Institute of Physics Pub., Bristol, 1998.
- 3. P. C. Liewer. Measurements of microturbulence in tokamaks and comparisons with theories of turbulence and anomalous transport. *Nuclear Fusion*, 25, 543–621, 1985.
- E. Mazzucato. Small-scale density fluctuations in the adiabatic toroidal compressor. *Physical Review Letters*, 36, 792–4, 1976.
- 5. E. Mazzucato. Low-frequency microinstabilities in the plt tokamak. *Physics of Fluids*, 21, 1063–9, 1978.
- C. M. Surko and R. E. Slusher. Study of the density fluctuations in the adiabatic toroidal compressor scattering tokamak using co/sub 2/ laser. *Physical Review Letters*, 37, 1747–50, 1976.
- R. E. Slusher and C. M. Surko. Study of density fluctuations in the alcator tokamak using co/sub 2/ laser scattering. *Physical Review Letters*, 40, 400– 403, 1978.
- 8. A. Hasegawa and K. Mima. Pseudo-three-dimensional turbulence in magnetized nonuniform plasma. *Physics of Fluids*, 21, 87–92, 1978.
- 9. A. Hasegawa, C. G. Maclennan, and Y. Kodama. Nonlinear behavior and

- turbulence spectra of drift waves and rossby waves. *Physics of Fluids*, 22, 2122–9, 1979.
- P. H. Diamond, S. I. Itoh, K. Itoh, and T. S. Hahm. Zonal flows in plasmaa review. Plasma Physics and Controlled Fusion, 47, R35–161, 2005.
- 11. M. G. Shats and W. M. Solomon. Experimental evidence of self-regulation of fluctuations by time-varying flows. *Physical Review Letters*, 88, 045001/1-4, 2002.
- 12. M. Jakubowski, R. J. Fonck, and G. R. McKee. Observation of coherent sheared turbulence flows in the DIII-D tokamak. *Physical Review Letters*, 89, 265003/1–4, 2002.
- G. R. McKee, R. J. Fonck, M. Jakubowski, K. H. Burrell, K. Hallatschek, R. A. Moyer, W. Nevins, D. L. Rudakov, and X. Xu. Observation and characterization of radially sheared zonal flows in DIII-D. *Plasma Physics and Controlled Fusion*, 45, A477–85, 2003.
- S. Coda, M. Porkolab, and K. H. Burrell. Signature of turbulent zonal flows observed in the DIII-D tokamak. *Physical Review Letters*, 86, 4835–8, 2001.
- A. Fujisawa, K. Itoh, H. Iguchi, K. Matsuoka, S. Okamura, A. Shimizu, T. Minami, Y. Yoshimura, K. Nagaoka, C. Takahashi, M. Kojima, H. Nakano, S. Ohsima, S. Nishimura, M. Isobe, C. Suzuki, T. Akiyama, K. Ida, K. Toi, S. I. Itoh, and P. H. Diamond. Identification of zonal flows in a toroidal plasma. *Physical Review Letters*, 93, 165002/1–4, 2004.
- Y. Hamada, A. Nishizawa, T. Ido, T. Watari, M. Kojima, Y. Kawasumi, K. Narihara, and K. Toi. Zonal flows in the geodesic acoustic mode frequency range in the JIPP T-IIU tokamak plasmas. *Nuclear Fusion*, 45, 81–8, 2005.
- G. D. Conway, B. Scott, J. Schirmer, M. Reich, and A. Kendl. Direct measurement of zonal flows and geodesic acoustic mode oscillations in ASDEX upgrade using doppler reflectometry. *Plasma Physics and Controlled Fusion*, 47, 1165–85, 2005.
- P. H. Diamond, M. N. Rosenbluth, F.L. Hinton, M. Malkov, J. Fleischer, and A. Smolyakov. Dynamics of zonal flows and self-regulating drift-wave turbulence. In 17th IAEA Fusion Energy Conference, volume IAEA-CN-69, page TH3/1, Yokohama, Japan, 1998. International Atomics Energy Agency, Vienna, 1998.
- H. Punzmann and M. G. Shats. Formation and structure of transport barriers during confinement transitions in toroidal plasma. *Physical Review Letters*, 93, 125003/1-4, 2004.
- K. W. Gentle. Diagnostics for magnetically confined high-temperature plasmas. Reviews of Modern Physics, 67, 809

  –36, 1995.
- N. Bretz. Diagnostic instrumentation for microturbulence in tokamaks. Review of Scientific Instruments, 68, 2927–64, 1997.
- 22. N. Hershkowitz. *Plasma Diagnostics*, volume 1 of *Plasma-materials interactions*. Academic Press, Boston, 1989.
- P. C. Stangeby and G. M. McCracken. Plasma boundary phenomena in tokamaks. Nuclear Fusion, 30, 1225–379, 1990.
- S. L. Chen and T. Sekiguchi. Instantaneous direct display system of plasma parameters by means of triple probe. *Journal of Applied Physics*, 36, 2363–75,

1965.

- E. J. Powers. Spectral techniques for experimental investigation of plasma diffusion due to polychromatic fluctuations. Nuclear Fusion. 14, 749–52, 1974.
- P. H. Diamond and Y. B. Kim. Theory of mean poloidal flow generation by turbulence. *Physics of Fluids B (Plasma Physics)*, 3, 1626–33, 1991.
- R. E. Waltz. Magnetic fluctuations, ambipolarity, charge filamentation, and plasma rotation in tokamaks. *Physics of Fluids*, 25, 1269–78, 1982.
- T. E. Stringer. Neoclassical transport in the presence of fluctuations. Nuclear Fusion, 32, 1421–32, 1992.
- W. M. Solomon and M. G. Shats. Nonambipolarity of fluctuation-driven fluxes and its effect on the radial electric field. *Physical Review Letters*, 87, 73–6, 2001.
- I. H. Hutchinson. Principles of plasma diagnostics. Cambridge University Press, Cambridge, New York, 1987.
- 31. W. M. Solomon and M. G. Shats. Fluctuation studies using combined mach/triple probe. *Review of Scientific Instruments*, 72, 449–52, 2001.
- W. M. Solomon, M. G. Shats, D. Korneev, and K. Nagasaki. Collective microwave scattering diagnostic on the H-1 heliac. Review of Scientific Instruments, 72, 352-4, 2001.
- 33. R. Nazikian, G. J. Kramer, and E. Valeo. A tutorial on the basic principles of microwave reflectometry applied to fluctuation measurements in fusion plasmas. *Physics of Plasmas*, 8, 1840–55, 2001.
- B. B. Afeyan, A. E. Chou, and B. I. Cohen. The scattering phase shift due to bragg resonance in one-dimensional fluctuation reflectometry. *Plasma Physics* and Controlled Fusion, 37, 315–27, 1995.
- 35. G. D. Conway, L. Schott, and A. Hirose. Plasma density fluctuation measurements from coherent and incoherent microwave reflection. *Plasma Physics and Controlled Fusion*, 38, 451–66, 1996.
- G. D. Conway, L. Schott, and A. Hirose. Comparison of reflectometer fluctuation measurements from experiment and two-dimensional numerical simulation. Review of Scientific Instruments, 67, 3861–70, 1996.
- M. Hirsch and E. Holzhauer. Doppler reflectometry with optimized temporal resolution for the measurement of turbulence and its propagation velocity. Plasma Physics and Controlled Fusion, 46, 593-609, 2004.
- G. McKee, R. Ashley, R. Durst, R. Fonck, M. Jakubowski, K. Tritz, K. Burrell, C. Greenfield, and J. Robinson. The beam emission spectroscopy diagnostic on the DIII-D tokamak. Review of Scientific Instruments, 70, 913–16, 1999.
- G. R. McKee, C. Fenzi, R. J. Fonck, and M. Jakubowski. Turbulence imaging and applications using beam emission spectroscopy on DIII-D (invited). Review of Scientific Instruments, 74, 2014–19, 2003.
- 40. T. P. Crowley. Rensselaer heavy ion beam probe diagnostic methods and techniques. *IEEE Transactions on Plasma Science*, 22, 291–309, 1994.
- 41. A. Fujisawa, H. Iguchi, S. Lee, T. P. Crowley, Y. Hamada, S. Hidekuma, and E. Kojima. Active trajectory control for a heavy ion beam probe on the compact helical system. *Review of Scientific Instruments*, 67, 3099–107,

1996.

- R.H. Kraichnan. Inertial ranges in two-dimensional turbulence. Physics of fluids, 10(7), 1417, 1967.
- 43. W Horton and Y.H. Ychikawa. Chaos and Structures in Nonlinear Plasmas. World Scientific, Singapore, 1996.
- 44. A. Hasegawa and M. Wakatani. Self-organization of electrostatic turbulence in a cylindrical plasma. *Physical Review Letters*, 59, 1581–4, 1987.
- Y. C. Kim and E. J. Powers. Digital bispectral analysis of self-excited fluctuation spectra. *Physics of Fluids*, 21, 1452–3, 1978.
- Y. C. Kim and E. J. Powers. Digital bispectral analysis and its applications to nonlinear wave interactions. *IEEE Transactions on Plasma Science*, PS-7(2), 120–31, 1979.
- 47. Y. C. Kim, J. M. Beall, E. J. Powers, and R. W. Miksad. Bispectrum and nonlinear wave coupling. *Physics of Fluids*, 32(2), 258–63, 1980.
- 48. V. Kravtchenko-Berejnoi, F. Lefeuvre, D. Krasnossel'skikh, and D. Lagoutte. On the use of tricoherent analysis to detect non-linear wave-wave interactions. Signal processing, 42, 291–309, 1995.
- W.B. Collis, P.R. White, and J.K. Hoammond. Higher-order spectra: the bispectrum and trispectrum. *Mechanical systems and signal processing*, 12(3), 375–94, 1998.
- C. P. Ritz and E. J. Powers. Estimation of nonlinear transfer functions for fully developed turbulence. *Physica D*, 20D(2-3), 320–34, 1986.
- 51. C. P. Ritz, E. J. Powers, and R. D. Bengtson. Experimental measurement of three-wave coupling and energy cascading. *Physics of Fluids B-Plasma Physics*, 1(1), 153–63, 1989.
- C. P. Ritz, E. J. Powers, R. W. Miksad, and R. S. Solis. Nonlinear spectral dynamics of a transitioning flow. *Physics of Fluids*, 31(12), 3577–88, 1988.
- 53. J. S. Kim, R. D. Durst, R. J. Fonck, E. Fernandez, A. Ware, and P. W. Terry. Technique for the experimental estimation of nonlinear energy transfer in fully developed turbulence. *Physics of Plasmas*, 3(11), 3998–4009, 1996.
- A. Hasegawa and K. Mima. Stationary spectrum of strong turbulence in magnetized nonuniform plasma. *Physical Review Letters*, 39(4), 205–8, 1977.
- 55. F. J. Crossley, P. Uddholm, P. Duncan, M. Khalid, and M. G. Rusbridge. Experimental study of drift-wave saturation in quadrupole geometry. *Plasma Physics Controlled Fusion*, 34(2), 235–62, 1992.
- P.J. Duncan and M.G. Rusbridge. The 'amplitude correlation' method for the study of nonlinear interactions of plasma waves. *Plasma Physics Controlled Fusion*, 35, 825–35, 1993.
- 57. H. Xia and M. G. Shats. Inverse energy cascade correlated with turbulent-structure generation in toroidal plasma. *Physical Review Letters*, 91, 155001/1–4, 2003.
- 58. H. Xia and M. G. Shats. Spectral energy transfer and generation of turbulent structures in toroidal plasma. *Physics of Plasmas*, 11, 561–71, 2004.
- J. Sommeria. Experimental study of the two-dimensional inverse energy cascade in a square box. *Journal of Fluid Mechanics*, 170, 139–68, 1986.
- 60. J. Paret and P. Tabeling. Intermittency in the two-dimensional inverse cas-